UNIVERSIDAD DE CANTABRIA

Facultad de Ciencias

POLARIZACIÓN DE LÁSERES DE CAVIDAD VERTICAL (VCSELs) SOMETIDOS A INYECCIÓN ÓPTICA PARALELA

(Polarisation of vertical-cavity surface-emitting lasers (VCSELs) subject to parallel optical injection)

Trabajo de Fin de Grado
para acceder al

GRADO EN FÍSICA

Autor: Alexandra Paola Popp

Director: Angel Valle Gutiérrez

Enero - 2016

En este trabajo investigamos la polarización de la luz emitida por un láser de cavidad vertical (VCSEL) sujeto a inyección óptica paralela de luz proveniente de otro laser.

En la primera parte del trabajo medimos las características del VCSEL emitiendo en solitario. Investigamos propiedades clave del VCSEL para medir algunos de los parámetros que caracterizan el funcionamiento del dispositivo. Encontramos una corriente umbral $I_{\mathrm{th}} = 1.618 \pm 0.014\,\mathrm{mA}$ con saturación a corrientes cercanas de los 9 mA, una eficiencia cuántica interna de $\eta = 0.1882 \pm 0.0006$, encendidos de polarización y biestabilidad óptica interna dependiente de la corriente aplicada. Encontramos un rango de longtitudes de orden del operación entre 1540 - 1544.5 nm y mediante la medida de los picos de oscilaciones de relajación de sistema encontramos una ganancia de $G_N = (1.64 \pm 0.2) \cdot 10^4\,\mathrm{Hz}$.

En la segunda parte del trabajo inyectamos luz de un láser sintonizable en un VCSEL usando un circulador óptico de tres puertos. Medimos la polarización dominante (llamada paralela) y la perpendicular a la anterior (llamada ortogonal). Encontramos una evolución lineal anticorrelacionada de las potencias de ambas polarizaciones dependiendo de la potencia inyectada de acuerdo al modelo presentado en el capitulo 2. Presentamos un mapa del régimen de bloqueo a la inyección y encendido de polarización (IL+PS). Investigando el comportamiento cuando se aumenta y se disminuye la potencia de inyección encontramos biestabilidad en la frontera entre las regiones de bloqueo a la inyección y IL+PS. La evolución de la potencia de las polarizaciones de salida al cambiar la desintonía en frecuencia se muestra como no lineal, en acuerdo con el modelo utilizado. De nuevo la frontera anterior se puede identificar como biestable en la mapa de estabilidad. Investigando como la polarización depende de la corriente aplicada al VCSEL confirmamos cualitativamente las predicciones teóricas.

palabras clave: VCSEL, encendido de polarización, inyección óptica paralela

In this work we investigate the polarisation of vertical-cavity surface-emitting lasers (VCSELs) subject to parallel optical injection from a master laser.

In the first part of the work we measure the characteristics of the free running VCSEL. Key properties of the used VCSEL have been investigated in order to measure some of the laser parameters that characterize the device performance. We find a threshold current of $I_{\mathrm{th}} = 1.618 \pm 0.014\,\mathrm{mA}$ with saturation at about 9 mA, an internal quantum efficiency of $\eta = 0.1882 \pm 0.0006$ and polarisation switching and internal optical bistability dependent on the bias current. For all possible bias currents we find a wavelength range of operation between 1540 - 1544.5 nm and by measuring the relaxation oscillation peaks of the system a differential gain of $G_N = (1.64 \pm 0.2) \cdot 10^4\,\mathrm{Hz}$ has been estimated.

In the second part of the work, we inject light from a tuneable laser via a three port optical circulator into a VCSEL and measure the dominant polarisation (denoted parallel) and the one perpendicular to it (denoted orthogonal). We observe an anticorrelated linear power evolution for both polarisations depending on the input current according to the model presented in chapter 2 and present a map of the injection locking and polarisation switching (IL+PS) regime. Investigating the behaviour when increasing and decreasing the injected power we find bistability in the boundary between IL+PS and complete injection locking. The power evolution of the output polarisations when varying the frequency detuning could be shown to be nonlinear in agreement with the used model. Again the boundary between injection locking and IL+PS could be identified as bistable in a stability map. Measuring the polarisation evolution dependence on the VCSEL bias current we qualitatively confirm the theoretical predictions.

Keywords: VCSEL, polarisation switching, parallel optical injection

Contents

1 Introduction

Only very recently, in 2014, the Nobel prize in physics was awarded to Isamu Akasaki, Hiroshi Amano and Shuji Nakamura for *the invention of efficient blue light-emitting diodes which has enabled bright and energy saving light sources.* This is only one of the many awards for semiconductor technologies but it reminds us of the importance of semiconductor devices in our daily life. The invention of the blue LED has triggered a transformation of lighting technology and made it possible to have energy saving, bright and long lasting light sources. It also reminds us, that there are still challenges in semiconductor research.

This work focuses on another, but less well known semiconductor device: the vertical-cavity surface-emitting laser (VCSEL). Invented in 1977 [1] it today holds the second largest production volume of all semiconductor lasers [2] but is still rather unknown to the public. It took 17 years for the devices to become commercialized. The first application for VCSELs back then in 2004 were optical computer mice, which still is a large field of application today [2]. However, their main applications today lie in optical signal transmission in local area networks, where data transmission rates up to tens of Giga-Bits per second can be achieved [2, 3]. In this sector, mainly 850, 1300 and 1550 nm devices are used.

In this work our objective is to investigate the polarisation of the light emitted by a long wavelength VCSELs subject to parallel optical injection from a master laser. The work is divided into four parts. We give theoretical background about semiconductor lasers and VCSELs in particular as well as optical injection and the expected output evolutions are considered. Furthermore a brief introduction on optical fibers is presented. In the second part our experimental equipment is presented and a characterisation of the used VCSEL is conducted. Methods, setup details and results are shown in the third part of the work. We discuss the dependence of the polarisation-resolved output power of the optical injection setup on the injected power, the frequency detuning and the bias current and also consider optical bistability. In the last chapter a summary and an outlook on the generality of our findings is given.

2 Theoretical Background

In this chapter, a theoretical introduction to relevant concepts and theoretical models is given. First the general semiconductor laser is introduced before going into detail on vertical-cavity surface-emitting lasers (VCSELs). Basic concepts of optical injection and optical fibers are presented.

2.1 Semiconductor LASER

There are three possibilities for light-matter interaction. Spontaneous emission, stimulated emission and absorption. The key process for semiconductor lasers, like for all lasers, is stimulated emission. Stimulated emission is an interaction between a photon $h\nu$ and an electron in the upper level of a system. When the photon passes the excited electron it can cause downconversion. This downconversion leads to the emission of a clone photon of our initial one. These two photons can now interact with more excited electrons, leading to amplification of the initial radiation. This amplification can however only take place if the photons encounter a sufficient amount of excited electrons. Therefore a pump source is used to ensure population inversion. [4]

Characteristic for a semiconductor is its band gap between valence band ($E < E_v$) and conduction band ($E > E_c$). In a semiconductor laser, the two states of the system involved in laser operation are energy levels from the conduction band and the valence band, respectively. Interaction can only occur for $h\nu > E_g$.

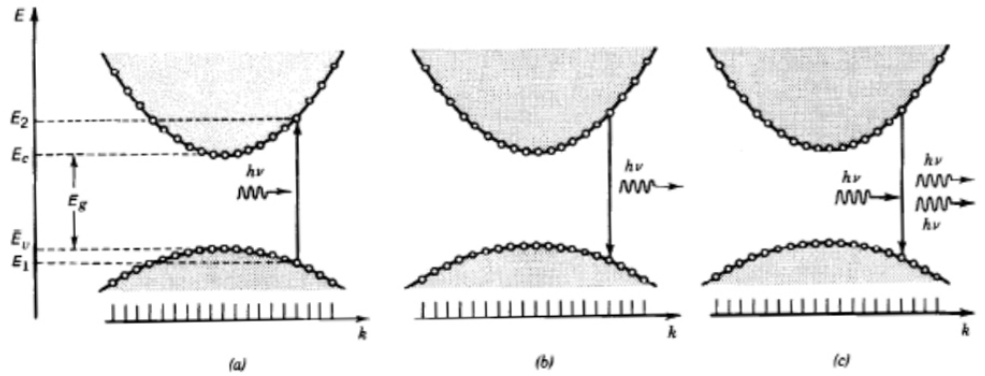

Figure 2.1: Possible light matter interactions for a semiconductor. a) absorption, b) emission c) stimulated emission [5]

The active medium of semiconductor lasers is usually heterostructured layers with a pn junction with current in the forward direction.When the current is large enough, there is a sufficient number of electrons in the conduction band to provide light amplification. Due to the high electron density in semiconductors a very high gain can be achieved and already small cavity distances on the order of $\sim 1\,\text{mm}$ are possible [4]. Cavity mirrors for semiconductor lasers are the crystal surfaces itself, which can be enhanced using additional Bragg mirrors directly grown on both sides of the active material. For a GaAs semiconductor with an emission at $\lambda = 850\,\text{nm}$ and an refractive index of $n = 3.5$ reflectivities on the order of 30% can be achieved. The gain from the pn junction is however sufficient to produce laser radiation even for a loss of 70% per turn. [4]

We can distinguish two types of semiconductor lasers, depending on the direction of the active medium in relation to the emitted light beam. For edge emitting devices the active medium is parallel to the light beam while for vertical emitters the active medium is orthogonal to the light beam. A comparison between edge emitters and VCSELs can be found in figure 2.4.

2.2 VCSEL

Vertical-cavity surface-emitting lasers are vertical semiconductor emitters which means that their active medium is orthogonal to the emitted laser radiation. They were invented by Kenichi Iga in 1977 [1] and currently hold the second largest production volume among all types of semiconductor lasers while recently being subject to intensive research [2]. VCSEL wavelengths of 414 - 2400 nm have been achieved [2]. In this work we will focus on so called long wavelength VCSELS emitting at around 1500 nm. These are of particular interest because the glass material of optical fibers has a significantly low absorption at this wavelength and it is thus popular within optical telecommunications.

2.2.1 Structure and Characteristics

There are three common possibilities to fabricate long wavelength VCSELs, using either GaInAs/InP, AlGaInAl/AlGaInAs or GaAs systems [1]. A schematic scheme of a VCSEL is presented in figure 2.2. The VCSEL is mounted on a metallic contact (1). The bottom mirror (2) is usually an n-doped DBR with a reflectivity on the order of 99.5%, while the top mirror (6) is a p-doped DBR. Doped mirrors are used in order to reduce ohmic losses and achieve a higher conductivity [6]. The mirror reflectivity needs to be higher than in the case of edge emitters, due the vertical structure with a very short cavity length. They usually consist of alternating GaAs and AlAs layers [6]. The VCSEL is electrically pumped by a current in forward direction of the pn junction by a current source. As an active medium, a quantum well is used. The vertical structure and high reflectivity mirrors allow to build structures even smaller than for edge emitters. Cavity length is on the order of $1\,\mu\text{m}$ [6] while complete devices can be as small as few μm in all directions [5]. VCSELs can be multimode or single mode devices.

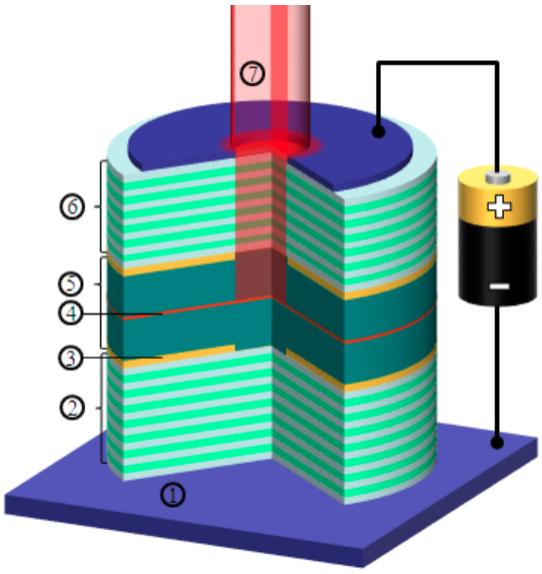

Figure 2.2: Schematic scheme of a VCSEL. 1 metallic contact 2 bottom mirror 3 oxidised layer 4 active medium 5 cavity 6 top mirror 7 laser emission [5]

The standard rate equation model for a linearly polarised single-mode semiconductor laser can be used to derive the temporal evolution of the light emitted by these devices [7]:

$$\begin{aligned} \frac{d\mathtt{P}}{dt} &= G_N(N - N_t)\,\mathtt{P} - \frac{\mathtt{P}}{\tau_P} + R_{\mathrm{sp}}(N) \\ \frac{dN}{dt} &= \frac{I}{e} - R(N) - G_N(N - N_t)\,\mathtt{P} \end{aligned} \tag{2.1}$$

where $\mathtt{P}$ is the number of photons in the cavity, N is the number of carriers in the active region, G_N is the differential gain, N_t is the number of carriers at transparency, τ_P is the photon lifetime, $R_{\mathrm{sp}}(N)$ is the spontaneous emission rate coupled to the laser mode, I is the bias current, e the electron charge and $R(N)$ the carrier recombination rate. Further specifications regarding the functions $R_{\mathrm{sp}}(N)$ and $R(N)$ can be found in reference [7].

From equations 2.1 the relaxation oscillation frequency ν_R and the damping rate Γ_R of the relaxation oscillations can be derived [7]. They are given by

$$\begin{aligned} \nu_R &= \sqrt{\frac{G_N}{e}(I - I_{\mathrm{th}})} \\ \Gamma_R &= \frac{1}{2}\left(\frac{1}{\tau_n} + \frac{G_N\,\tau_p}{e}(I - I_{\mathrm{th}})\right) \end{aligned} \tag{2.2}$$

where τ_n is the differential carrier lifetime at the lasing threshold. Relaxation oscillations are oscillations that arise from the periodic interaction between the population inverted

level of the laser and the electric field inside the cavity [6]. They appear when the system departs from its steady state due for instance to a change in the bias current driving the laser and get damped over the operation time. A scheme of the change in current, population and output power is presented in figure 2.3.

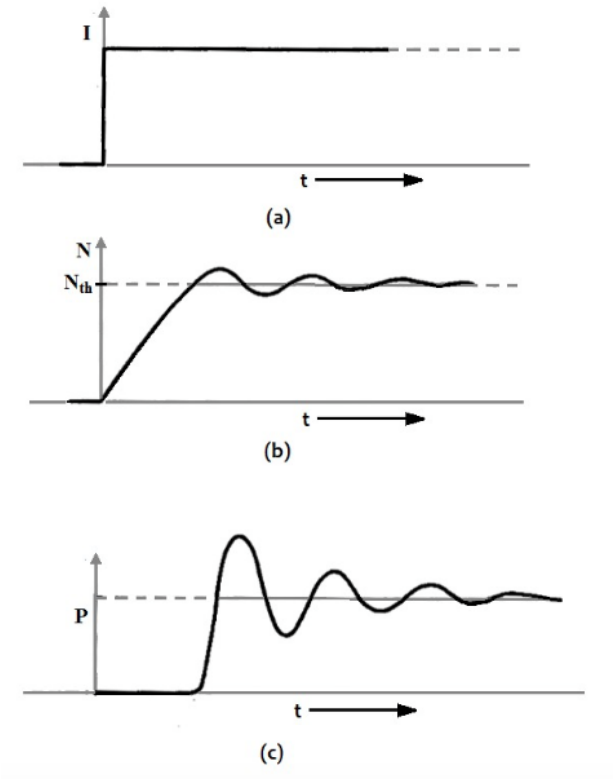

Figure 2.3: Damped relaxation oscillations caused by a change in current (a) in the population, (b) the number of photons and (c) the power [8]

The optical power emitted by a laser is directly proportional to the number of photons emitted. Following from equations 2.1 in which we assume steady state, hence $\frac{dN}{dt} = \frac{d\mathtt{P}}{dt} = 0$ an expression of the optical power can be derived as:

$$P = \eta \cdot \frac{h\nu}{e}(I - I_{\text{th}}) \tag{2.3}$$

where P is the power emitted by the VCSEL, η is the internal differential quantum efficiency, h is the Planck constant, ν is the frequency the VCSEL is emitting at, I is the bias current corresponding to the output P and I_{th} is the threshold current [8]. Following this equation, the internal differential quantum efficiency of a device is the ratio of the number of photons in the light beam to the carriers above threshold. When the output power P and applied current I to a VCSEL are measured while the frequency ν and the threshold current I_{th} are known, η can be estimated.

2.2.2 Advantages and Applications

Todays the main application for VCSELs lie in near and midrange optical communications. They are becoming key devices for LAN [1] especially for metropolitan areas and wide area networks [3]. State of the art 2013, transmission rates of up to 25 GBits/s were predicted [2]. However in 2014 already rates of 46 Gbits/s have been reported [9].

Features of vertical emitters are low power consumption together with a high speed modulation and low driving current. The narrow circular beam can be used for direct fiber coupling [3] or applications where only simple beam shaping optics are desirable. Devices are also characterised by high reliability and accurately predictable lifetimes on the order of 10 million hours at room temperature [2].

Diverse applications for VCSELs arise from the possibility of having single-mode emission with one linearly polarised quasi-Gaussian transverse mode as well as continuous wavelength tuning available just by changing cavity dimensions [2].

The advantages of VCSELs compared to the other two most common semiconductor devices, edge emitters and LEDs, are listed in table 2.1. Schemes of the three devices in comparison are presented in figure 2.4.

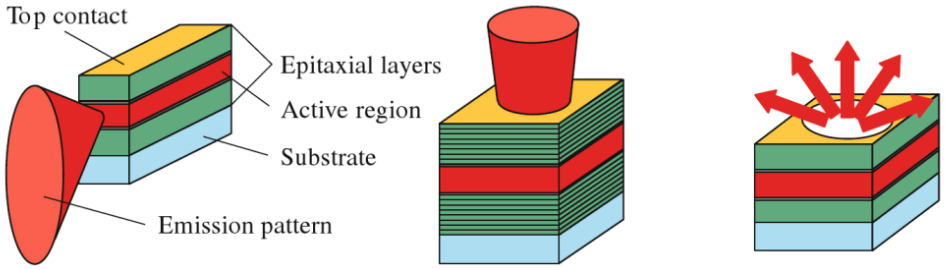

Figure 2.4: Edge emitting device (left), VCSEL (center), LED (right) [2]

VCSEL vs. edge emitter	VCSEL vs. LED
+ low threshold current	+ high modulation bandwidth
+ circular beam profile output	+ circular beam profile output
+ high power conversion efficency	+ high power conversion efficency
+ wafer-level testing	+ small operating current
+ simple mounting and packaging	+ high output power
+ possibility of 2d arrays	+ narrow spectrum

Table 2.1: VCSEL advantages against LEDs and edge emitters [2]

2.3 Optical Injection

Due to their high gain, low facet reflectivity and amplitude-phase coupling through the linewidth enhancement parameter α, semiconductor lasers are sensitive to optical injection from another laser [10]. Under certain conditions we can achieve optical injection locking (OIL) from this procedure. OIL signifies that the slave laser oscillation frequency equals that of the master laser. Also a constant phase difference between the electric fields of master and slave laser is obtained. It has been intentionally developed to control and stabilise laser oscillations, today the applications include intensity, frequency and partition noise reduction, microwave signal generation or the production of chaotic signals for secure communications and random number generation [10]. OIL can be achieved by injecting a single-mode signal from a master laser with a frequency difference between the signals of the two lasers on the order of GHz. This frequency difference is called detuning.

OIL locking for VCSELs has been subject to studies for some time, however only recently the attention has shifted to also considering polarised optical injection [11]. Our VCSEL has two linear polarisation modes, of which one is dominant in the free running operation. We call them parallel (X) and orthogonal (Y). The directions of X and Y electric fields are orthogonal and lie in the active region plane. We consider parallel optical injection as injecting linearly polarised light from the master laser with a polarisation parallel to the dominant linear polarisation of the VCSEL and orthogonal optical injection as injection with light orthogonally polarised to the dominant VCSEL polarisation direction. A schematic example of optical injection with corresponding terminology is given in figure 2.5.

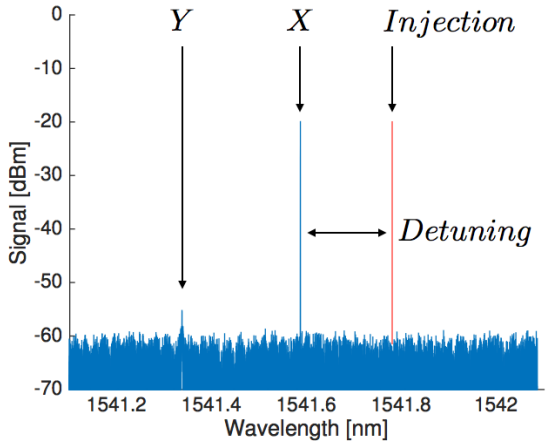

Figure 2.5: Scheme for optical injection. X dominant polarisation, injection (red) and detuning with respect to X. Parallel optical injection: polarisation of injected light parallel to X, orthogonal optical injection: polarisation of injected light orthogonal to X

Most experimental work so far has been dealing with orthogonal optical injection, only recently parallel optical injection in 1550 nm VCSELs has been studied and stability maps have been presented [11, 12]. Predominantly the phenomena of injection locking has been studied so far. Other phenomena such as polarisation switching (PS) or periodic dynamics and a period-doubling route to chaos are however also possible depending on the injection conditions. Polarisation switching is a phenomena, where under certain conditions the dominant polarisation can change. In a VCSEL with two linear polarisation directions, where initially X is the dominant and Y is suppressed, after PS, Y is dominant and X is suppressed. This is illustrated in figure 2.6.

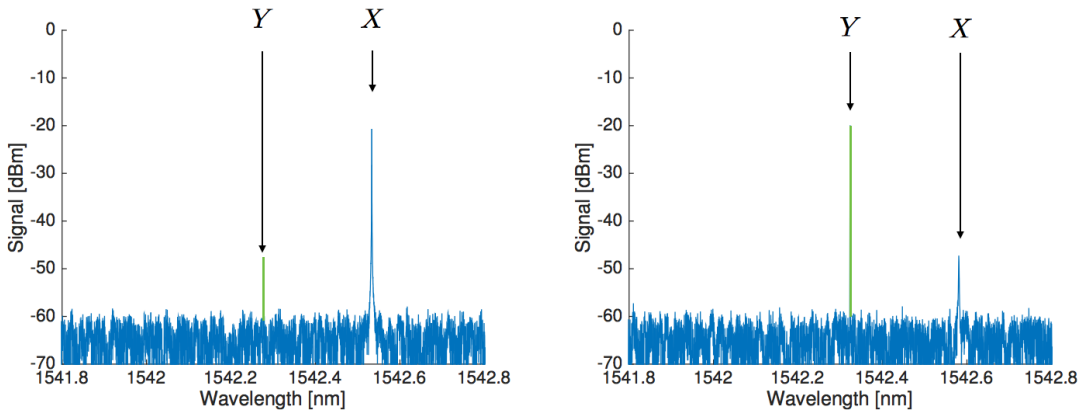

(a) Parallel polarisation dominant, orthogonal suppressed

(b) Orthogonal polarisation dominant, parallel suppressed

Figure 2.6: Schematic plot of polarisation switching. (a) X dominant, Y suppressed after PS (b) Y dominant, X suppressed

An extension of the model 2.1 to a VCSEL with two linear polarisation modes under parallel optical injection is given in [13]. A variety of dynamical states is found in [13]. A new state in which the X polarisation is locked to the injection and the Y polarisation of the VCSEL is excited is predicted in [13]. We call it IL+PS state. A similar state has also been predicted very recently by using a similar model of edge-emitter semiconductor lasers subject to optical injection [14]. This work also includes analytical expressions in order to analyse the stability of this solutions. Figure 3 of reference [14] gives the regions in the plane detuning vs injected power in which this solution is stable and hence can be observed. In order to calculate the theoretically expected behaviour, we use the approach from reference [14] and expressions (10), (11) and (12) of reference [13], which describe the evolution of X and Y in dependency of the power injected into the slave laser P_{inj} and the frequency detuning denoted by ν_i:

$$\mathcal{P}_{\mathrm{x}} = \left(\frac{\kappa}{2\gamma_a}\right)^2 \cdot \frac{P_{\mathrm{inj}}}{1 + \left(\frac{\pi\nu_i}{\gamma_a} + \alpha\right)^2} \tag{2.4}$$

$$\mathcal{P}_{\mathrm{y}} = \frac{\mu}{1 - \frac{\gamma_a}{\kappa}} - \mathcal{P}_{\mathrm{x}} \tag{2.5}$$

$$\phi_{\mathrm{x}} = \arctan\left(\frac{\pi\nu_i}{\gamma_a} + \alpha\right) \tag{2.6}$$

where κ is the field decay rate, γ_a the linear dichronism, α the linewidth enhancement factor and μ the normalised bias current [15]. $\mathcal{P}_{\mathrm{x}}$ is the normalised output power of the parallel polarisation, $\mathcal{P}_{\mathrm{y}}$ of the orthogonal. ν_i is the frequency detuning, P_{inj} the power injected into the VCSEL and ϕ_{x} the phase difference of the electrical fields between the VCSEL and the master laser.

2.4 Optical Fibers

An optical fiber consists of a core, a cladding and a polymer jacket, as shown in figure 2.7a. The refractive index of the respective layer decreases from inside to outside. Usually optical fibers are made from a core of doped silica (glass) and a cladding of pure silica.

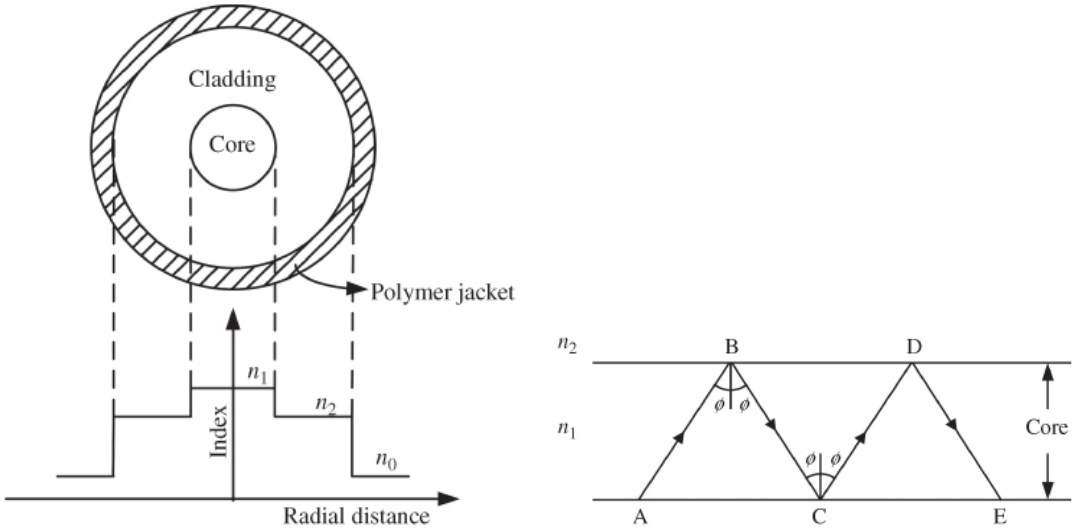

(a) Schematic drawing of an optical fiber [16] (b) Propagation of light in an optical fiber [16]

Figure 2.7: Setup and rey propagation of fibers

Signal transmission in optical fibers is based on total internal reflection. A scheme of the propagation is shown in figure 2.7b. We have a core with an refractive index n_1, a

cladding with refractive index n_2 and a critical angle ϕ_c. The incoming light ray with an angle $\phi > \phi_c$ undergoes total internal reflection at point B, then at point C and like this at all following core to cladding interfaces. Like this it continues to the end. Total internal reflection is characterised by the fact that the $R =$ reflected power/incident power $= 1$ [16]. When using Snell's law

$$\begin{aligned} n_1 \sin(\phi_{\text{in}}) &= n_2 \sin(\phi_{\text{trans}}) \\ \sin(\phi_{\text{in}}) &= \frac{n_2}{n_1} \sin(\phi_{\text{trans}}) \end{aligned} \tag{2.7}$$

we can derive the critical angle for $\sin(\phi_{\text{trans}}) = 1$, hence

$$\phi_{\text{in}} = \phi_c = \arcsin\left(\frac{n_2}{n_1}\right). \tag{2.8}$$

When using fibers in experiments, we have to consider two possible types of connectors distinguished by their ferrule polishing, angled physical contact (APC) and physical contact (PC). Connection schemes are shown in figure 2.8. APC connectors have an $8\,^\circ$ cutoff in their ferrules in order to make a tighter connection and to decrease the reflected power at the connector [17]. It is not possible to directly connect PC to APC without inducing extra losses.

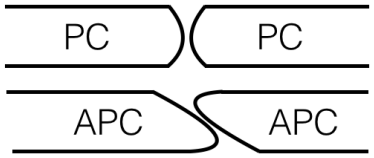

Figure 2.8: Connection scheme for APC and PC connectors

3 Characterisation of the free running Device

In this chapter components of the setup used for the following measurement are presented along with a characterisation of the used single mode VCSEL. All measurements are performed at a temperature of $T = 25.00 \pm 0.05\,^{\circ}\mathrm{C}$.

3.1 Description and Characteristics of the experimental Equipment

In this section, setup elements and analysers used for this work are presented. At first the used VCSEL and its controllers are introduced, then our analysers are described and in the end of this section all components connected with the fiber optics in our setup will be presented.

3.1.1 VCSEL

We employ a commercial singlemode VCSEL (RayCan) with an emission range of approximately 1540 - 1545 nm. Detailed analysis of the specifications of the laser is given in the later part of this chapter. A scheme of our VCSEL is presented in figure 3.1.

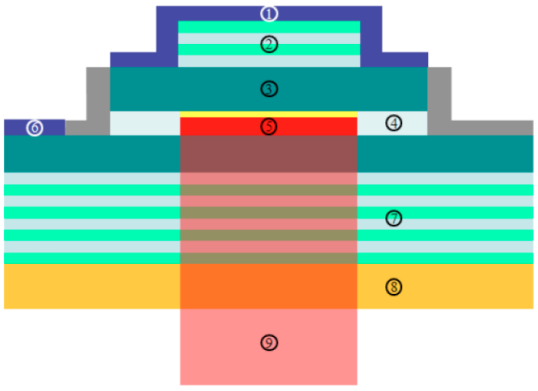

Figure 3.1: Schematic structure of our VCSEL: 1 top contact 2 top mirror 3 InP spacer 4 current confienment 5 active medium 6 bottom contact 7 bottom mirror 8 InP substrate 9 emitted light [6]

It is fabricated on a InP substrate with an active region of height 0.5λ, where λ is the wavelength of the light inside the device, and consists of multiple quantum wells. The active medium is placed in between two n-InP plates, which are used to decrease electric resistance. Top and bottom mirrors are made from layers of InAlAs/InAlGaAs. [6]

The VCSEL current is controlled by a Thorlabs *LDC202B* laser diode controller. The controller allows input precision of 0.001 mA in a range from 0 to 20 mA. It handles the Thorlabs *TCLDM9* laser diode mount which typically operates in a temperature range from 5 - 70 °C. The temperature control of the mount is operated by the Thorlabs *TED 200* temperature controller that allows an input precision of 0.01°C and permanent temperature surveying. Operating temperature ranges from 0 - 40 °C. When monitoring the active temperature due to external influences, a real $\Delta T = 0.05$°C is however more reasonable.

3.1.2 Analysers

High resolution optical spectrum analyser (BOSA)

The Aragon Photonics *BOSA 210* is used for optical spectral analysis. It uses stimulated Brillouin scattering spectroscopy for optical spectrum analysis. The Brillouin response of a tuneable laser with a continuously changing wavelength over a desired spectral range is measured to obtain the desired spectrum in high resolution [18]. A maximum resolution of 10MHz at an 80 dB dynamical range can be obtained. The tuneable laser allows high sweep speeds in order to obtain nearly instantaneous measurement results. Due to internal heating of the tuneable laser, the device should undergo a *run* and *stop* procedure before each measurement when measuring absolute wavelength values to avoid shifting of the spectra.

Optical Spectrum Analyser (OSA)

For higher amplitude resolution optical spectrum analysis the Anritsu *MS9710B* diffraction-grating spectrum analyser is used. The OSA operates within a wavelength range of 600 - 1750 nm with a precision of $\Delta\lambda = \pm 0.05$ nm ($\Delta\nu = \pm 6.3$ GHz). Minimum resolution is 0.07 nm. It can resolve amplitudes in a range of -90 - +10 dBm with an accuracy of $\Delta P = 0.4$ dB (videobandwidth 10 Hz for 10 times sweep averaging) [6]. It therefore has a higher amplitude but lower wavelength resolution than the BOSA.

Photodetector (PD)

A photodetector produces an output voltage pulse proportional to an optical input signal that can be processed by analysers. We use the Thorlabs *PDA8GS*, which is a InGaAs PIN photodiode coupled with a transimpedance amplifier. Our device has a bandwidth of 9 GHz and a peak response of 0.95 A/W at 1550 nm.

Microwave Spectrum Analyzer (MSA)

The Microwave Spectrum Analyzer Anritsu *MS2719B* is used to monitor the microwave emission spectra of our VCSEL. Input are electrical impulses from a photodetector. It measures the intensity of certain frequencies in a range from 9 kHz to 20 GHz. It provides an output of signal strength in dBm.

Fiber-optic power meter (PM)

We use multiple Thorlabs *PM20* fiber-optic power meter to record output powers of our lasers. The device has a InGaAs sensor. The measurable optical power ranges from -60 dBm to 20 dBm, the covered wavelength range is 400 - 1700 nm. Measurements can be conducted in dBm or W, with a measurement uncertainty of $\Delta P = \pm 0.25$ dB. Signal input is via direct fiber connection.

Attenuator

We use the OZ Optics Digital Variable Attenuator *DA-100*. It allows direct input of the desired attenuation in dB through a keypad. The attenuator works by block type, which means that a blocking device is inserted into a beam of collimated light from the source fiber. The angle of the blocking device is depending on the desired attenuation [19]. The device allows attenuation from 0 - 60 dB.

Tuneable Laser

The external cavity semiconductor tuneable laser Anritsu *Tunics Plus* is used in our experiments. It can be tuned in a wavelength range from 1500 - 1625 nm with a minimum resolution of 1 pm and a maximum output power of 8 mW. The device consists of a diode laser, a dihedral reflector and a diffraction grating. Its tuneability is achieved by rotating the reflector around a center of rotation, so that the ratio of cavity length to wavelength is kept constant. [6]

3.1.3 Fiber optical components

Fiber Polarisation controller (FPC)

We use the Fiber U-Bench polarisation controller Thorlabs *FBR05*. It consists of three waveplates which are placed between two fiber collimators. The two outer waveplates correspond to $\lambda/4$, while the inner plate corresponds to $\lambda/2$. The desired polarisation can be selected by rotating the waveplates against each other. Due to their mode of operation fiber U-Bench polarisation controllers are more stable than looped fiber controllers.

Fiber Optical Circulator

We use a non-polarisation maintaining fiber optical circulator from Newport with a center wavelength of 1550 nm. Our circulator has three ports. A schematic plot is presented in

figure 3.2. When light enters port 1 it can only exit through port 2. When it enters port 2 it can only exit port 3 and when it enters port 3, it will suffer a large amount of losses in ports 1 and 2. Fiber optical circulators are non-reciprocal, which means that changes induced in the light by traveling in one direction are not reversed when traveling in the other [6].

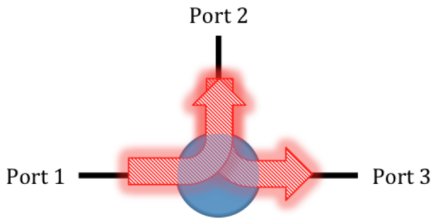

Figure 3.2: Schematic scheme of a 3 port optical circulator [6]

Polarisation Beamsplitter

We use the Newport *F-PBC-15-SM-FA* polarisation beam combiner/splitter. The device can be used to combine light from two fibers into one single fiber or split the signal of one fiber into its parallel and orthogonal polarisation components. The device has a center operation wavelength of 1550 nm. The ratio of parallel to orthogonal polarisation loss is 2.25 dB.

Optical Fiber 50/50 Coupler

We use the Newport *F-CPL-F12155* optical fiber 50/50 coupler. The device has a center operation wavelength of 1550 nm, return loss of 55 dB and a maximum insertion loss of 3.4 dB.

3.2 Dependency of VCSEL output Power on applied Current

In order to characterise the device, at first a measurement of the output power depending on the driving current of the VCSEL is conducted. Two different situations are monitored, first the VCSEL is directly connected to a power meter (PM) and the total output power independent of the polarisation is measured. In a second step the VCSEL output is first sent into a polarisation controller (PC) and from there into a bench fiber with a rotating linear polariser before entering the PM.

3.2.1 Polarisation Independent

The results of the polarisation independent measurement can be seen in figure 3.3.

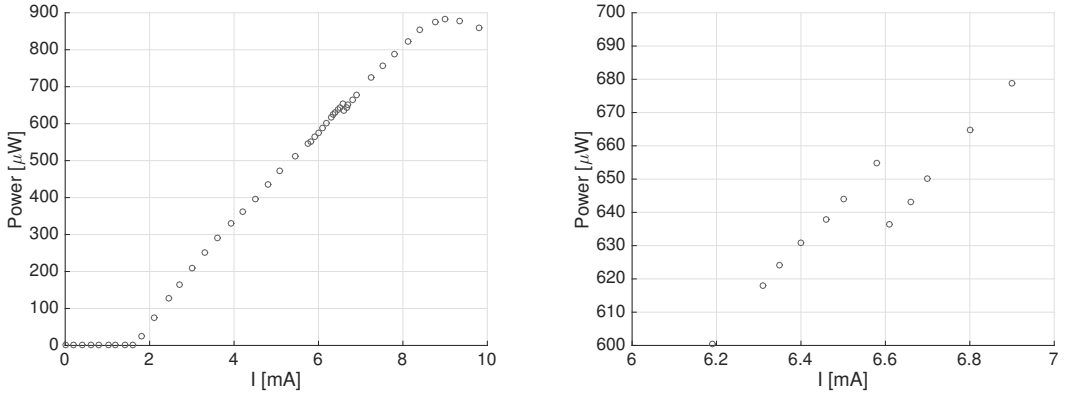

(a) Full Measurement (b) Detail

Figure 3.3: Measurement of the total output power over a range of different bias currents

As expected very small output is present underneath the threshold current. Through a linear fit the threshold could be determined as $I_{\mathrm{th}} = 1.618 \pm 0.014\,\mathrm{mA}$, which is in agreement with previous measurements for this device [20]. After the threshold the output power increases linear until about 6.4 mA. From figure 3.3b (Detail) it can be seen that a drop in the total power of about $20\,\mu\mathrm{W}$ appears at this point. This drop arises when switching from a dominant polarisation (denoted as parallel) to a polarisation with smaller gain (denoted as orthogonal) is occurring. We choose in the optical spectrum that parallel (orthogonal) polarisation is corresponding to the longer (shorter) wavelength. After the switch, operation is again linear before reaching saturation at about 9 mA.

From this measurement, the internal quantum efficiency for the transformation of electric to optical power can be determined using equation 2.3. We compute $\eta = 0.1882 \pm 0.0006$ by a fit of P over $(I - I_{\mathrm{th}})$. This value is in agreement with previous measurements for this device [20].

3.2.2 Polarisation Dependent

Now, the VCSEL output is first sent through a polarisation controller (PC) before passing a bench fiber and the PM. We choose $I = 5\,\mathrm{mA}$ for emission in parallel direction. The linear polariser in the bench fiber is set to 0 degrees perpendicular to the optical tabel and the polarisation is adjusted to a minimum. All measurements now correspond to a state where only the orthogonal polarisation is present. For measurements of the parallel polarisation, the polariser is set to 90 degrees perpendicular to the optical tabel. Measurements of the two polarisations for one current are taken successively. Results can be

obtained from figure 3.4, where I is given in a linear scale, while for P_a a logarithmic scale is chosen. Spectra corresponding to figure 3.4 taken with the BOSA are given in figure 3.6.

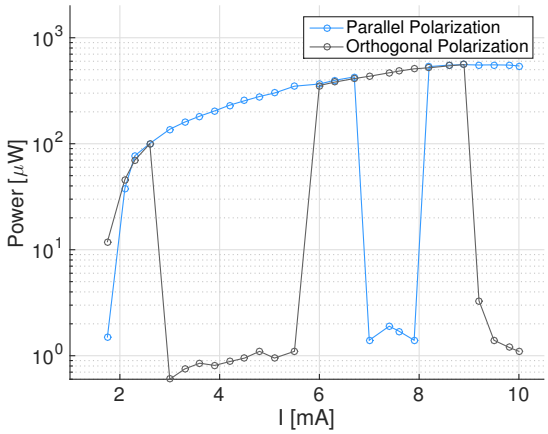

Figure 3.4: Polarisation dependent measurement of the output power over a range of different driving currents

Right after the threshold current, the orthogonal polarisation is dominant for a short range followed by a period where both polarisations are active over a range of about 1 mA. Then the orthogonal polarisation switches off and the parallel becomes the dominant one over a range of about 3 mA. In theory the inferior polarisation is supposed to stay constant while the dominant polarisation increases. Due to the logarithmic scale of our graphical representation we discover, that there is a slight trend of increase in the inferior polarisation. This behaviour occurs, due to imperfect polarisation alignment between the direction of the linear polariser and the direction of the linear polarisation of the VCSEL. Before and after each measurement the polarisation is switched from one state (either 0° or 90°) to the other. This manual alignment is however not in a way that zero intensity in the inferior polarisation can be achieved. Hence, while the power in the dominant polarisation increases this polarisation contaminates the inferior. With increase of the dominant polarisation we see an increase of this contamination through out the measurement. Also baseline jumps can be explained by the fact that new polarisation alignment is done for each measurement, due to this the alignment may vary slightly between measurements. Close to 6 mA the dominant polarisation switches from the parallel to the orthogonal polarisation. This result is in agreement with the result from section 3.2.1 where we studied an effect in the total power due to a switch where the inferior polarisation becomes the dominant one. The parallel polarisation is switched back to the dominant position at about 8 mA and stays dominant until saturation is reached.

During all polarisation switchings we observe several currents where both polarisations are of equal value corresponding to the value of the previously dominant polarisation, independent of the kind of switching. Consistently this should go along with peaks in figure 3.3, which is not the case. If we look at the optical spectrum at some of the values where this behaviour occurs, we observe jumps between two stable states. This phenomenon is qualitatively presented in figure 3.5 where two different polarisation states for the same bias current $I = 6.4\,\mathrm{mA}$ are shown. Both spectra were taken with the same parameters. Figure 3.5a was recorded right after setting the parameters. After waiting for a short time the polarisation state changed due to noise resulting in figure 3.5b. The slight decrease in wavelength from figure 3.5a to b is most probably due to the heating of the internal tuneable laser of the BOSA.

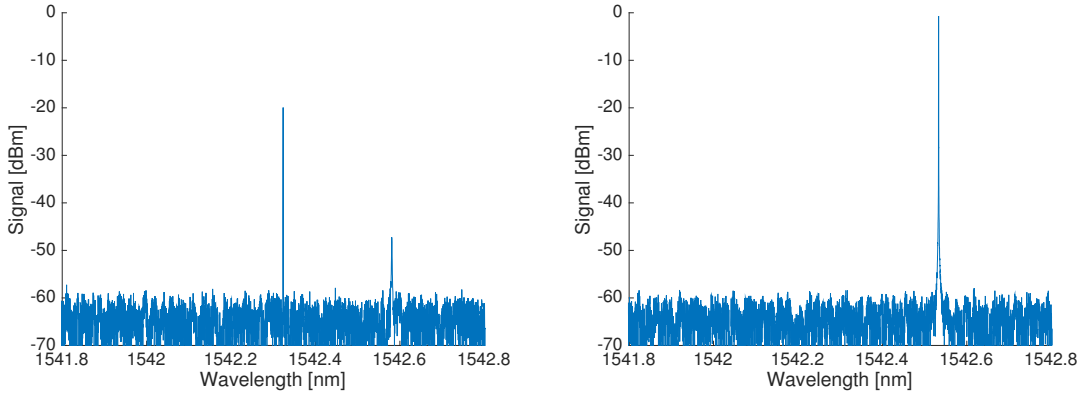

(a) Orthogonal polarisation dominant, parallel suppressed

(b) Parallel polarisation dominant, orthogonal not visible

Figure 3.5: Spectra for $I = 6.4\,\mathrm{mA}$ illustrating internal bistability of the VCSEL

The rate equations for the VCSEL predict internal optical bistability of our system in some regions [21]. If we go close to the boundaries of these regions, we do not only see stable polarisations but often instantaneous jumping between two polarisation states. Our only explanation for the behaviour in figure 3.4 lies in the way the PM measures at these points. As we see in our optical spectrum, jumps occur in a time scale of seconds. Readings in our power meter correspond to averages in much shorter scales. These readings change between a large and a small value. In figure 3.4 we have represented the large value. This is the reason why figure 3.4 is inconsistent with figure 3.3 in the bistable regions. A power average of low and large values in the bistable regions should be done to achieve consistency in future work.

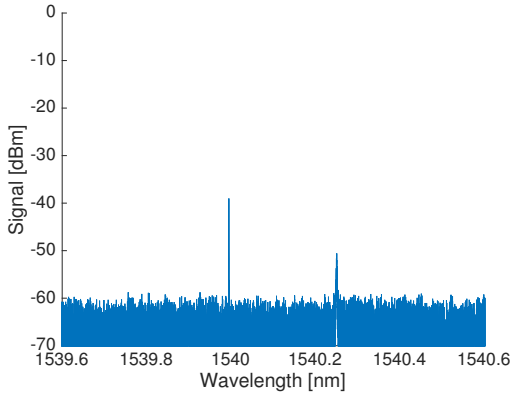

(a) $I = 1.8\,\mathrm{mA}$

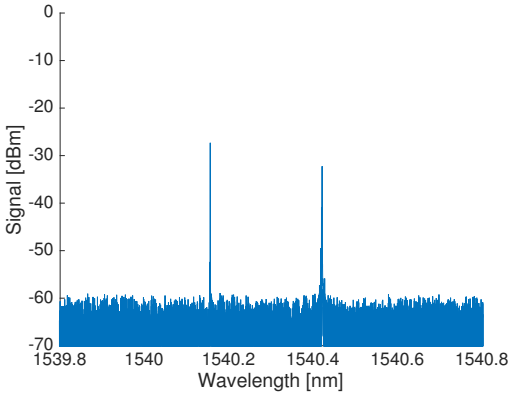

(b) $I = 2.3\,\mathrm{mA}$

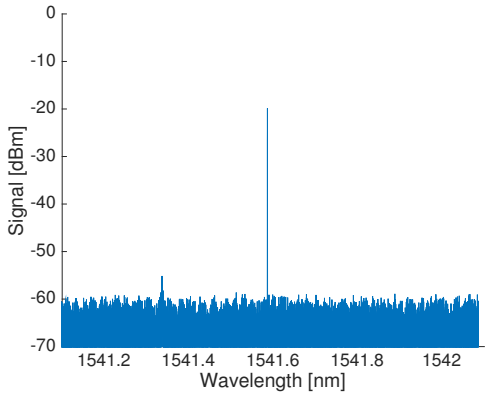

(c) $I = 4.5\,\mathrm{mA}$

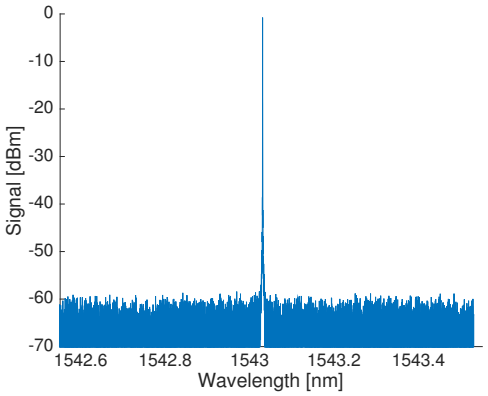

(d) $I = 7.3\,\mathrm{mA}$

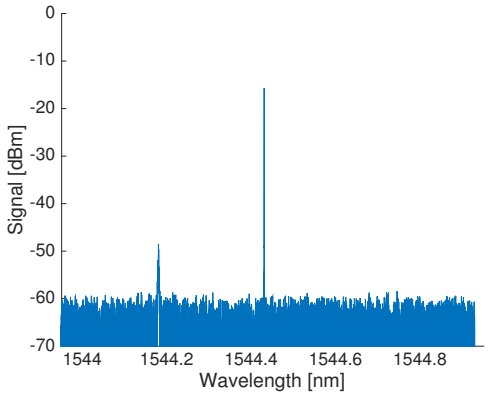

(e) $I = 9.0\,\mathrm{mA}$

Figure 3.6: Spectra corresponding to the total power over a range of different driving currents

3.3 Dependency of VCSEL output Wavelength on applied Current

Taking into account the previous results, an analysis of the output wavelength for a range of currents is conducted. Therefore the VCSEL is directly connected to the BOSA where the center wavelength of the spectra is measured for each current. When more than one peak is present in the spectrum, the one with the highest intensity is chosen. Results can be obtained from figure 3.7.

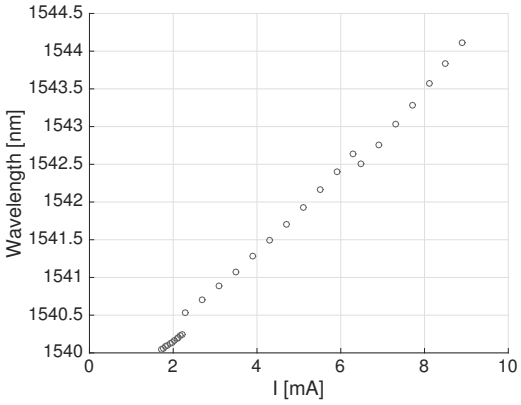

Figure 3.7: Measurement of the wavelength with maximum intensity over a range of different driving currents

Results show three different regions, now denoted as $\lambda_\mathbf{1}$, $\lambda_\mathbf{2}$ and $\lambda_\mathbf{3}$. The first region $\lambda_\mathbf{1}$ corresponds to the region before the first switching between I_{th} and about 3 mA, where the orthogonal polarisation is dominant. A linear increase is visible. Then a polarisation switch to the parallel polarisation takes place. This is consistent with our previous results. The wavelength of the parallel polarisation is greater than the one of the orthogonal and we measure a sudden jump in wavelength to a higher value. Again the increase is linear until 6 mA where another jump, this time to a lower wavelength, and hence a switch back to the orthogonal is visible. Increases in all three ranges can be considered linear. R^2 and slope values are given in table 3.1.

	$m \pm \Delta m$	R^2
$\lambda_\mathbf{1}$	0.391 ± 0.002	0.997
$\lambda_\mathbf{2}$	0.528 ± 0.009	0.998
$\lambda_\mathbf{3}$	0.668 ± 0.007	0.999

Table 3.1: Slope and R^2 values for output current ragnes $\lambda_\mathbf{i}$

From previous results [20], we thought that the slopes of the two polarisations should stay constant over the complete range of currents. Results from table 3.1 however show

that this is not the case. We see a constant increase of the slope from low to high current values. This discrepancy probably arises from the measurement procedure. In previous experiments, this measurement was conducted with the OSA, which offers a better amplitude resolution, hence both polarisation peaks have been visible throughout the whole range of currents. Slope fits previously were only conducted over the total range of currents. The measurement presented here was taken with the BOSA, therefore we trade a higher wavelength resolution for a lower amplitude resolution. Due to this it was not possible to monitor both polarisations throughout the complete range of currents, hence only the dominant one is plotted and hence three fits were done. These fits show that over the whole current range a single linear relation between λ and I does not hold.

3.4 Spectral Analysis and Relaxation Oszillations

To complete the characterisation of our device, the spectrum was analysed using the MSA in order to measure the relaxation oscillation frequency. Spectra for three different currents are presented in figure 3.8a, while the results following equation 2.2 are shown in figure 3.8b. Computed relaxation oscillation frequencies for different currents are given in table 3.2.

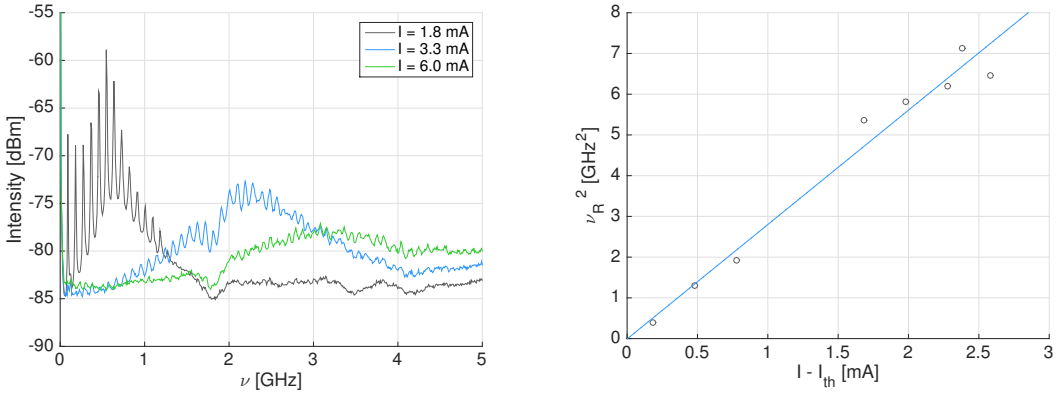

(a) Radiofrequency spectrum of the free running VCSEL for different currents

(b) Squared relaxation oscillation frequencies at different currents subtracted by threshold current

Figure 3.8: Radiofrequency spectra and obtained relaxation oscillation frequencies

The peak within each of the spectra in figure 3.8a corresponds to the relaxation oscillation frequency at the corresponding current. With increasing current the oscillation peaks shift further away from the initial signal. The spikes in the signal, most prominently visible for $I = 1.8\,\mathrm{mA}$ correspond to feedback from the cavity formed with the VCSEL mirrors and the tip of the fiber pigailed to the VCSEL. The fiber has a length of approximately 1 m. The corresponding frequency allowed for this cavity is $c_0/2nL$, where c_0 is the speed

of light in vacuum and n is the refractive index of the fiber (~ 1.5). Hence

$$\nu_{\text{reflection}} = \frac{c_0}{2nL} = \frac{3 \cdot 10^8 \, \frac{\text{m}}{\text{s}}}{2 \cdot 1.5 \cdot 1\,\text{m}} \sim 100\text{MHz} \tag{3.1}$$

This could be avoided by closing off remaining air in the connection between the output fiber of the VCSEL and our detector with special gel. We chose not to do so in order to avoid detector contamination. The 100 MHz peaks are reduced by FFT low pass filters with a cut-off frequency of 0.001 GHz. The smoothed data is then used for peak fitting.

In figure 3.8a a dip in all spectra is visible for $\nu \sim 1.8\,\text{GHz}$. This dip is an intrinsic malfunction of the RSA. It presents no problem for our analysis as long as it does not directly correspond to the location of the relaxation peak. Thus, measurements for 2.7 mA and 3.0 mA are not presented. A dependency of $\nu_R^2 = (2.6 \pm 0.3) \cdot (I - I_{\text{th}}) + 0.2$ with $R^2 = 0.971$ is found. Our data is not as good as in previous measurements [7], because we chose not to measure with the reflection reduced method. Thus it is harder to determine the true peak of the spectra due the reflection contamination which is visible in figure 3.8a. In order to calculate the differential gain G_N from our dataset we use eq. 2.2. Using the slope from figure 3.8a computed as (2.6 ± 0.3), we arrive at

$$G_N = (1.64 \pm 0.2) \cdot 10^4\,\text{Hz}. \tag{3.2}$$

Compared with previous results [8, 20] this value for G_N seem reasonable. Our computed error is however slightly larger than in previous cases. This high errors most probably arrive from the previously mentioned difficulties in the peak fitting process. Due to these difficulties also only very few points are observed which could also be a contribution to the higher error. In order to check the results, in figure 3.9 an optical spectrum at $I = 3.05\,\text{mA}$ is presented with a span of 8 GHz.

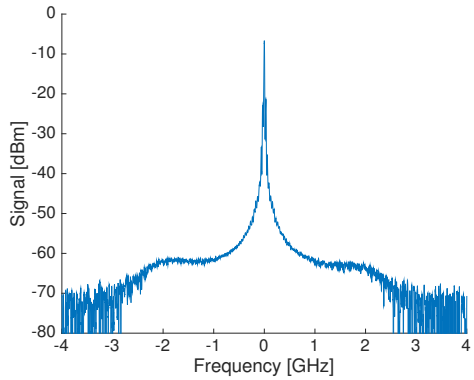

Figure 3.9: Optical spectrum at $I = 3.05\,\text{mA}$, span of 8 GHz. Center frequency shifted to 0 GHz.

Relaxation oscillation peaks appear as satellite peaks and should be located at $\nu_R \sim 2.0\,\mathrm{GHz}$, which is in agreement with our computed data which predicts $\nu_R = 1.5\,\mathrm{GHz}$.

I [mA]	1.8	2.1	2.4	3.3	3.6	3.9	4.2	4.5
ν_R [GHz]	0.62	1.15	1.39	2.39	2.41	2.49	2.67	2.54

Table 3.2: Computed relaxation oscillation frequencies after data smoothing

4 Method, Experimental Setup and Results

In this chapter we analyse the polarisation switching states of our VCSEL in an experimental way. Stability maps obtained by variation of injection power at a constant detuning and variation of the detuning at a constant injection power are presented. Variation of the bias current is also subject to our investigations.

4.1 Experimental Setup

We use an all-fiber setup shown in figure 4.1 to achieve parallel optical injection. Light from a tuneable master laser is injected into a 1550 nm VCSEL. The laser light is passed through a variable attenuator to adjust the injected power before the polarisation is selected with a polarisation controller. An APC/PC connection fiber is inserted in between the attenuator and the polarisation controller. We adjust polarisation in a way that injection is achieved in the same polarisation direction as the dominant VCSEL polarisation. Another PC/APC connector is installed after the controllers. Injection is realised by a three port optical circulator. The power injected into the VCSEL is measured with a 50/50 coupler directing half the injected power to a power meter. After port 3 of the optical circulator another polarisation controller is placed to select the parallel VCSEL polarisation as dominant. PC/APC connectors are placed before the signal passes through a polarising beamsplitter where the different polarisations are separated. Data acquisition is performed with either a power meter for each polarisation direction or our high resolution optical spectra analyser (BOSA).

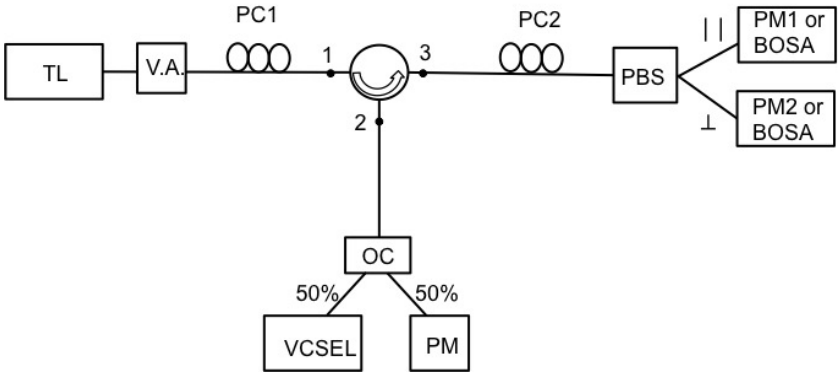

Figure 4.1: Experimental setup for parallel optical injection. TL tuneable laser, V.A. variable attenuator, PC1 and PC2 polarisation controllers, PBS polarising beamsplitter, OC optical coupler, PM power meter.

4.2 Dependence on the Injected Power

We choose a bias current of $I = 3.05\,\mathrm{mA}$ which is on the order of twice the threshold current. In the previous chapter we have seen, that according to measurements from sections 3.2.2 and 3.3 we do not observe any switching or intrinsic bistable behaviour at this current. Two spectra of our free running VCSEL at $I = 3.05\,\mathrm{mA}$ are given in figures 4.2, taken with BOSA and OSA, respectively.

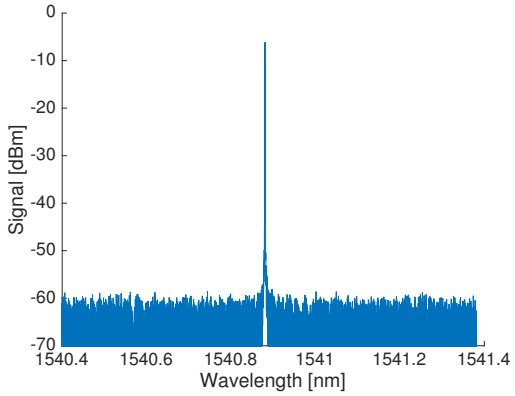

(a) BOSA spectrum

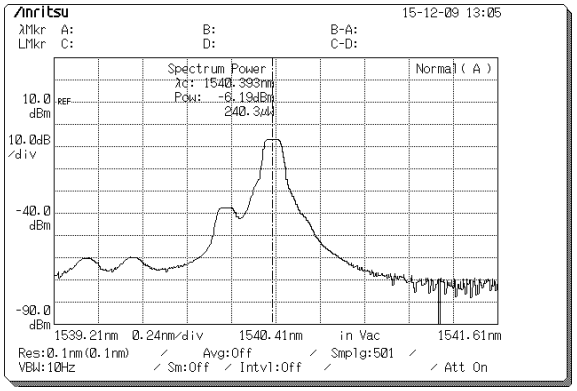

(b) OSA image

Figure 4.2: Free running VCSEL at $I = 3.05\,\mathrm{mA}$

In the BOSA spectrum we can only see one clear peak, which is the parallel (also denoted as x) polarisation of the VCSEL emitting at $\lambda = 1540.91\,\mathrm{nm}$. The OSA also shows us the suppressed orthogonal (also denoted as y) polarisation due to better amplitude resolution, which is shifted $0.26\,\mathrm{nm}$ to the short wavelength site and suppressed by about $30\,\mathrm{dB}$. Hence the birefringence of our VCSEL corresponds to $33\,\mathrm{GHz}$. We classify the parallel polarisation as the one that appears at a smaller frequency, and the orthogonal as the one that appears at the higher, when both are present. The two peaks on the left side of the OSA spectrum correspond to higher order transverse modes, which are not visible in the BOSA due to the limited resolution. The two slightly different center wavelengths in both pictures correspond to calibration differences between the two analysers.

4.2.1 Increasing Injected Power

At first we fix a detuning and increase the injected power in our system in order to classify different behaviours of the oscillator under parallel optical injection. Figure 4.3 shows the spectra for five different injected powers at a detuning of $\nu = -8.4\,\mathrm{GHz}$. The spectra are normalised in a way that the parallel polarisation of the free-running VCSEL defines $\nu = 0$. Our signal is the coherent addition of the VCSEL emission and the reflection of the optical injection from the front surface of the VCSEL.

For $P_{\mathrm{inj}} = 133\,\mu\mathrm{W}$ (4.3a) we observe periodic dynamics in the parallel polarisation and

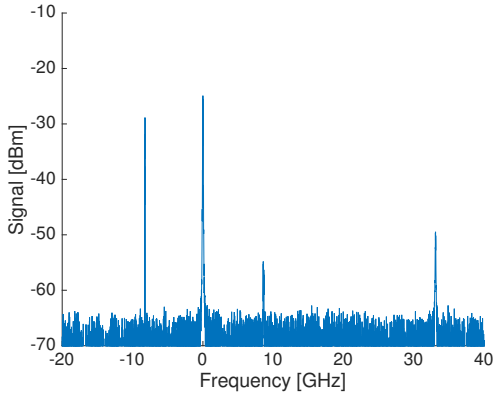

(a) $P_{\text{inj}} = 133\,\mu\text{W}$

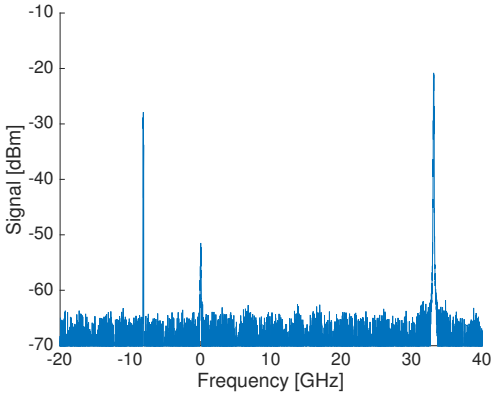

(b) $P_{\text{inj}} = 209\,\mu\text{W}$

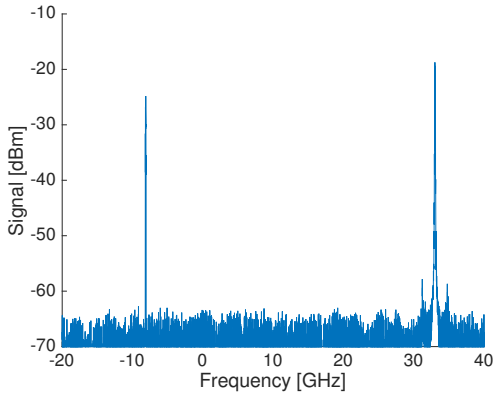

(c) $P_{\text{inj}} = 416\,\mu\text{W}$

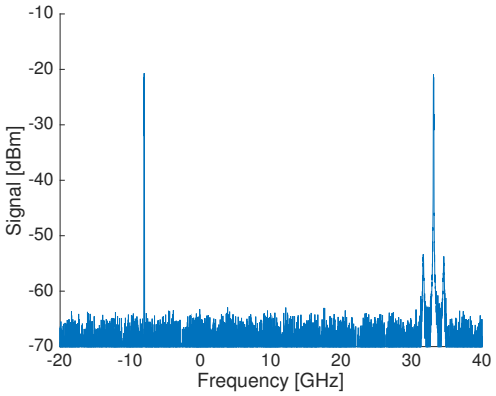

(d) $P_{\text{inj}} = 833\,\mu\text{W}$, averaged

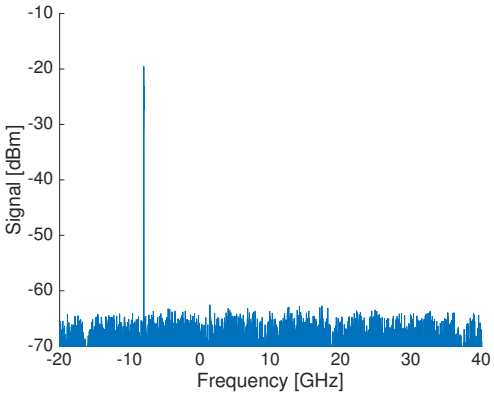

(e) $P_{\text{inj}} = 1056\,\mu\text{W}$

Figure 4.3: Spectra corresponding to different injected powers at a detuning of $\nu = -8.4\,\text{GHz}$. All spectra were obtained by using a sweep average, in order to obtain a better image of the relaxation oscillations. Slight peak broadening is seen in all figures due to this averaging.

already an excited orthogonal. With an increase of the total power these dynamics disappear and for $P_{\text{inj}} = 209\,\mu\text{W}$ (4.3b) we find the parallel polarisation slightly suppressed and an increase in the orthogonal. For $P_{\text{inj}} = 416\,\mu\text{W}$ (4.3c) the free-running parallel polarisation at 0 frequency is fully suppressed and the orthogonal fully excited. Figures 4.3a - c show that with an increase of the injected power the free-running parallel polarisation gets more and more suppressed while in the same time the orthogonal gains more energy. Figure 4.3c shows injection locking and polarisation switching achieved at the same time. We will denote this state as IL+PS. If we further increase the injected power (4.3d, $P_{\text{inj}} = 833\,\mu\text{W}$), we find a situation where the orthogonal polarisation is accompanied by two small peaks. These peaks deviate by 1.45 GHz from the main peak. These frequency peaks are close to relaxation oscillations, which should be located at 2.0 GHz. The polarisation switching is maintained for a range of injected powers, we find injection locking (IL) at $P_{\text{inj}} = 1056\,\mu\text{W}$ (4.3e). A complete theoretical description of this situation can be found in [13].

Now we measure the output power evolution over the injected power for several detunings. A complete set of measurement results for $\nu = -8.6\,\text{GHz}$ is presented in figure 4.4.

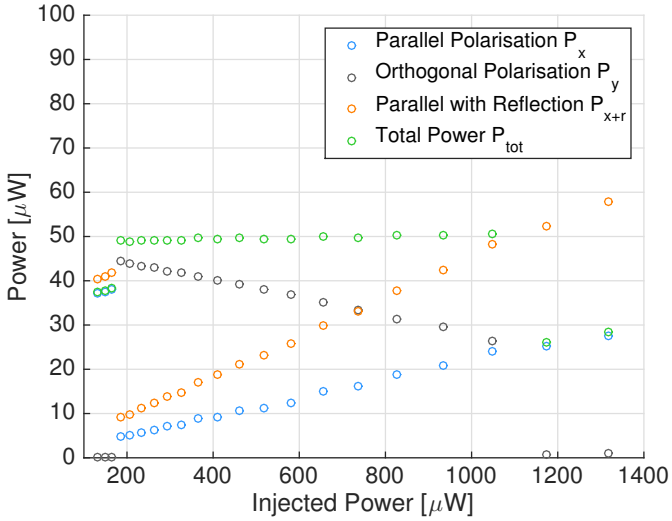

Figure 4.4: Output power evolution over injected power for $\nu = -8.6\,\text{GHz}$, IL+PS regime extends from $P_{\text{inj}} = 180\,\mu\text{W}$ to $P_{\text{inj}} = 1050\,\mu\text{W}$

For these measurements we have to take the reflection of the VCSEL into account. We fix a value of detuning and at the three different output ports of our system, we measure P_{inj}, $P_{\text{x+reflection}}$ (from now on denoted as $P_{\text{x+r}}$ or 'parallel with reflection') and P_{y}. In order to obtain the true power in the parallel polarisation P_{x}, we conduct in the following a second measurement where we turn the VCSEL off and just measure the power in the parallel port of the beamsplitter for different injected powers as shown in figure 4.5a. The reflected

power (from now on denoted as P_r) is linear with P_{inj}. We now compute $P_x = P_{x+r} - P_r$. This procedure can be applied, because following from equation 2.6 the phase difference the reflected injected light and the X polarisation equals 90°. Furthermore we multiply the orthogonal polarisation power P_y by 1.68 for all measurements. This is due to the ratio of parallel to orthogonal polarisation loss of 2.25 dB. Hence the true value of the power in the orthogonal polarisation is $P_y = P_{y,\,measured} \cdot 10^{(2.25/10)} = P_{y,\,measured} \cdot 1.68$.

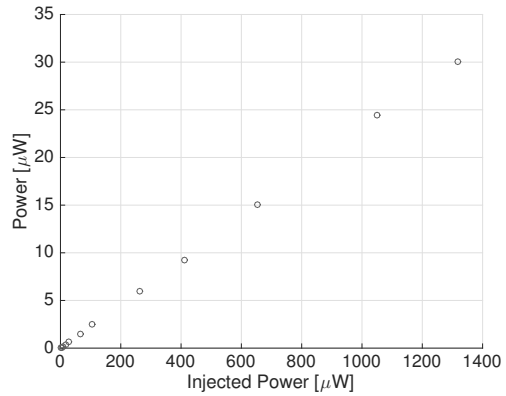

(a) Reflected power for parallel polarisation

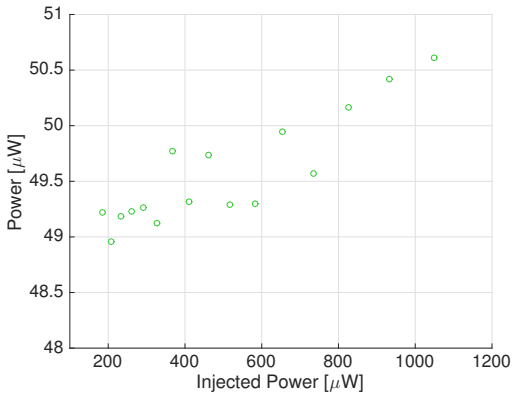

(b) Detail of the total power, IL+PS regime only

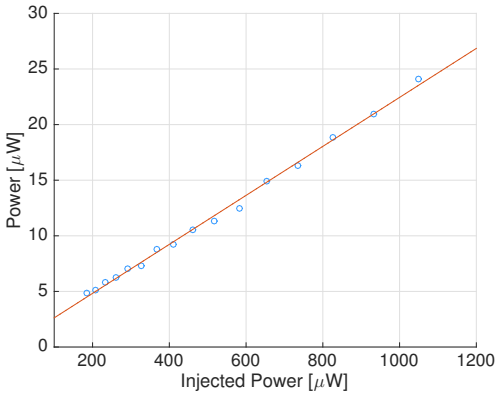

(c) Detail of P_x, IL+PS regime only

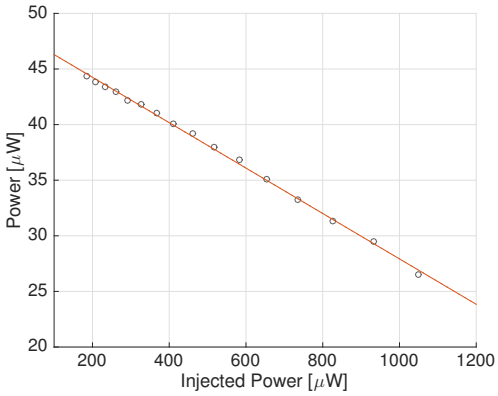

(d) Detail of P_y, IL+PS regime only

Figure 4.5: Power evolution over injected power for $\nu = -8.6\,\text{GHz}$, zooms of figure 4.4

Before the IL+PS regime, the total power as well as P_x respectively P_{x+r} emit at a power of about 40 μW. After the switching the total power increases to 50 μW. In theory we expect a constant total power along with a linear decrease of P_y and a linear increase of P_x in the IL+PS state according to equations 2.4 and 2.5. Linear fits for the P_x and P_y are presented in figure 4.5c and d. We find $R^2(P_x) = 0.9965$ and $R^2(P_y) = 0.9983$ hence we consider our data in agreement with the theoretically predicted linear behaviour. We see however a slight increase ($\sim 3\%$) of P_{tot} (figure 4.5b) along with the other expected behaviours. A trend for P_{tot} seems to be present in nearly all our measurements and

at this point we have no explanation for this deviation from theory. After switching to complete IL we detect again a decreased total power and nearly no activity in P_y.

In order to map the power evolution of our laser, we conduct several measurements for different detunings in a range of -11 to $+2\,\mathrm{GHz}$ for a range of P_{inj} up to $1.3 \cdot 10^3\,\mu\mathrm{W}$. All power evolutions for different regions follow the same scheme. Examples for $\nu = -5.0\,\mathrm{GHz}$ and $\nu = +1.7\,\mathrm{GHz}$ (only IL+PS regime, reflection corrected values) are presented in figure 4.6. We see that measurements from the different regions are in accordance with the one presented in figure 4.5 and hence conclude that our model seems to be agreeing with the measured results.

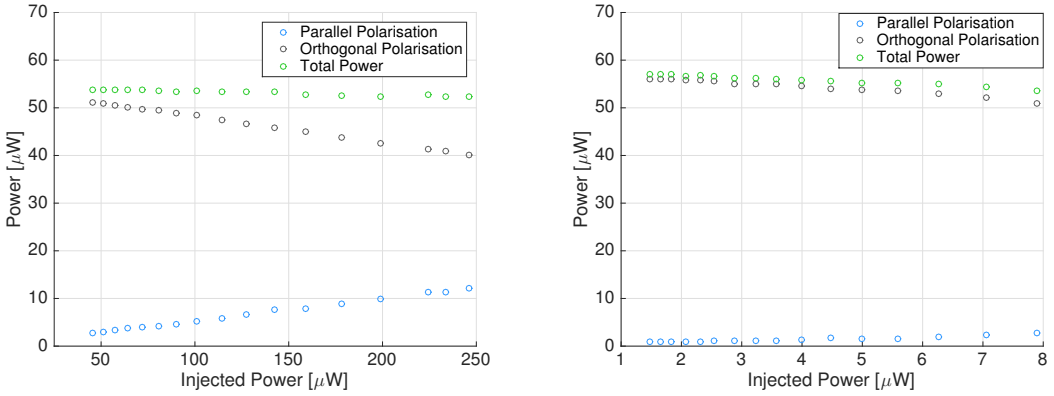

(a) Detuning $\nu = -5.0\,\mathrm{GHz}$

(b) Detuning $\nu = +1.7\,\mathrm{GHz}$

Figure 4.6: Power evolution over injected power, IL+PS regime only, parallel polarisation reflection reduced.

We use all these results to give a map of the IL+PS region of our VCSEL for $I = 3.04\,\mathrm{mA}$ (figure 4.7). We plot the injected power against the frequency detuning ν_i. Points correspond to the points where a switch in behaviour is seen. The enclosed area corresponds to the IL+PS regime. A theoretically computed stability map is given in figure 4.8. Details on the theoretical description of this system are given in [13].

Good qualitative agreement between theory and experiment is found. We identify a stable IL+PS region for our VCSEL for positive as well as negative detunings. The region for negative detunings is bigger than the region for positive values as expected. Smaller detunings, in both positive and negative regions are more difficult to measure because they are subject to less stable detunings and more chaotic behaviour is found. This makes a distinction between the different states more difficult. Admittedly in this work only the IL+PS state is analysed and a complete characterisation of other states of the system is subject to future investigations.

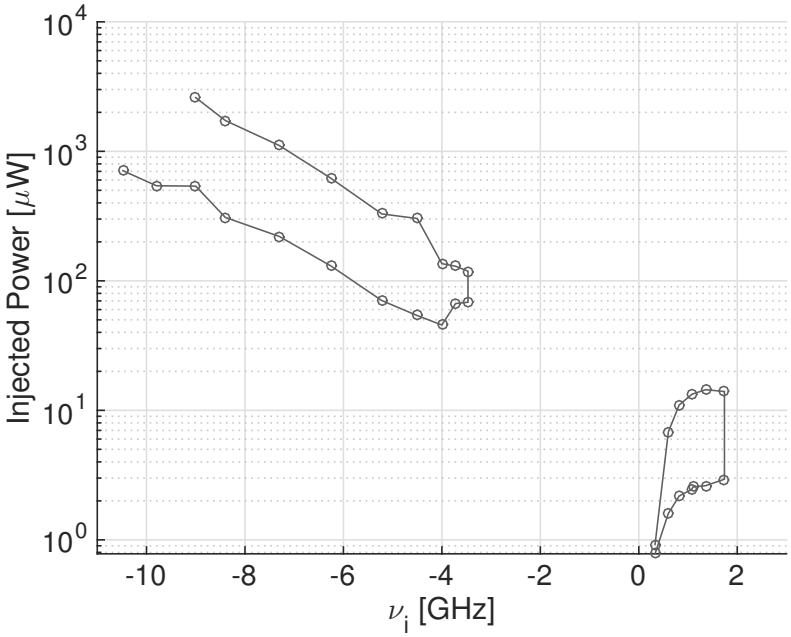

Figure 4.7: Map of the IL+PS region for $I = 3.05\,\mathrm{mA}$ obtained by increase of P_{inj} for fixed detunings. Injected power in logarithmic scaling.

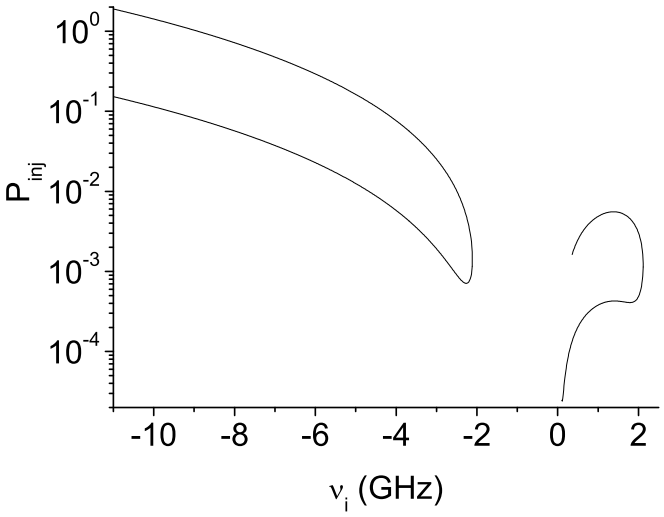

Figure 4.8: Theoretical map of the IL+PS region for $I = 3.05\,\mathrm{mA}$, injected power in logarithmic scaling obtained according to [13].

4.2.2 Decreasing Injected Power

In section 3.2.2 we show that our VCSEL itself is subject to optical bistability without an injecting system. Now we want to analyse the bistability of the IL+PS region. Therefore we conduct a similar measurement as before and now decrease P_{inj} (Figure 4.9). We choose only to investigate the negative detuning region because the total IL+PS regime is greater and more stable in this part.

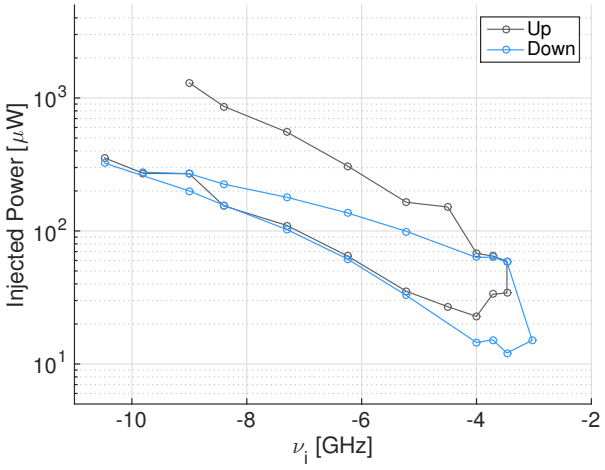

Figure 4.9: Map of the IL+PS region for $I = 3.05\,\mathrm{mA}$ obtained by decrease (blue, down) and increase (grey, up) of P_{inj} for fixed detunings.

We find that now our upper boundary of the IL+PS region is significantly shifted to lower injected powers for greater detunings. In this case the master laser is able to lock the VCSEL oscillation for smaller powers, once locking is already achieved. The rate equations (eq. 2.1) predict the upper boundary to be bistable, which is in agreement with our results. For detunings on the order of -4 GHz the locking regime is similar, it is even possible to achieve locking for a detuning where we did not observe locking in the case of power increase. For small detunings we also experience a shift of the lower boundary. The area of the IL+PS regime is decreased by a significant amount.

4.3 Dependence on the Frequency Detuning

We choose to investigate the dependency of the stability of our system on the change of the frequency detuning. Therefore we set again a bias current of $I = 3.05\,\mathrm{mA}$ and now fix the injected power while varying the detuning of our system. We concentrate on sweeping only the negative detuning region. We measure P_{inj} and P_{y} with PMs and P_{x} with the OSA because we see fluctuation in the parallel polarisation. The OSA allows us the possibility of direct sweep averaging. We reduce the reflection of the system again and multiply P_{y} by 1.68 due to the beamsplitter losses. P_{x} is manipulated to compensate for different calibrations of the OSA and the PMs.

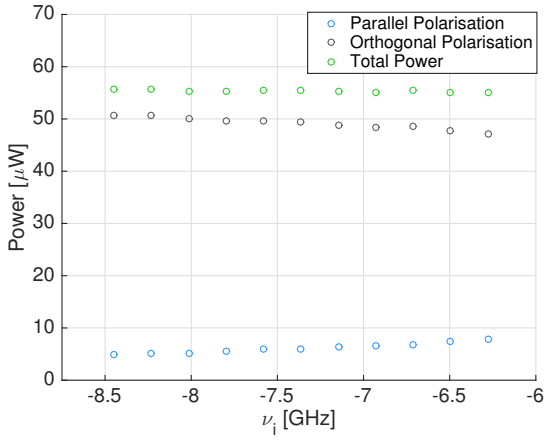

Figure 4.10: Power evolution over detuning for $P_{\text{inj}} = 151\,\mu\text{W}$, IL+PS regime only

A measurement for $P_{\text{inj}} = 151\,\mu\text{W}$ is presented in figure 4.10. During measurements the initial detuning is always decreased to obtain a minimum detuning in the end. For figure 4.10 a sweep average of 10 is conducted for every P_{x}. Again we expect a constant total power. Theory predicts curvature in the parallel as well as in the orthogonal polarisation accordingt to equations 2.4 and 2.5. Figures 4.11a and b show detailed pictures of parallel and orthogonal evolution, respectively. A linear slope fit shows the presence of curvature in the averaged P_{x} and P_{y} values. The P_{x} and P_{y} curves both cross the linear fit twice which supports the existence of some curvature in both polarisation. Measurements for other currents (figure 4.12) $P_{\text{inj}} = 39\,\mu\text{W}$ (4.12a, b) and $P_{\text{inj}} = 78\,\mu\text{W}$ (4.12c, d), respectively, show similar behaviour.

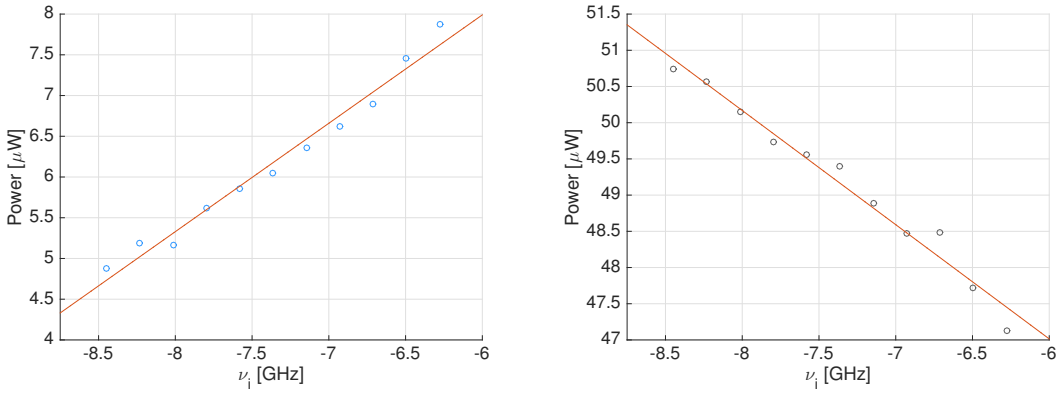

(a) Detail of P_{x}

(b) Detail of P_{y}

Figure 4.11: Power evolution over detuning for $P_{\text{inj}} = 151\,\mu\text{W}$, IL+PS regime only, Detail, zoom of figure 4.10

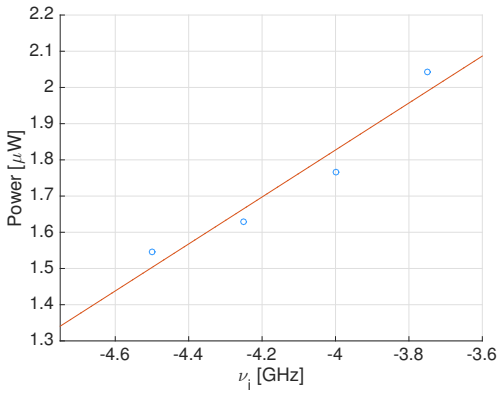

(a) $P_{\text{inj}} = 39\,\mu\text{W}$, detail of P_{x}

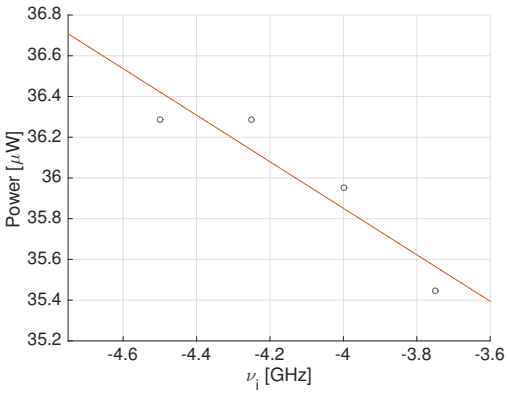

(b) $P_{\text{inj}} = 39\,\mu\text{W}$, detail of P_{y}

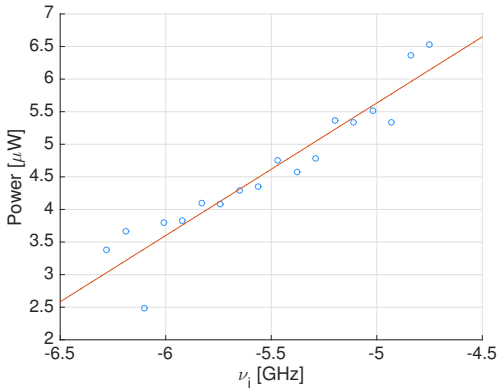

(c) $P_{\text{inj}} = 78\,\mu\text{W}$, detail of P_{x}

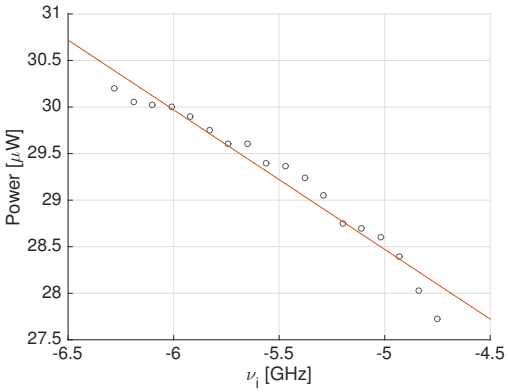

(d) $P_{\text{inj}} = 78\,\mu\text{W}$, detail of P_{y}

Figure 4.12: Power evolution over detuning for $P_{\text{inj}} = 39\,\mu\text{W}$ (a, b) and $P_{\text{inj}} = 78\,\mu\text{W}$ (c, d), IL+PS regime only, Detail

With the previous hints supporting our theoretical assumption of curvature, nonlinear regression fits of the data set for $P_{\text{inj}} = 151\,\mu\text{W}$ using eq. 2.4 and 2.5 are computed. Results are presented in figure 4.13.

Starting with equations 2.4 and 2.5 we use the relations $P_{\text{x}} = c \cdot \mathcal{P}_{\text{x}}$ and $P_{\text{y}} = c \cdot \mathcal{P}_{\text{y}}$ to link the normalised values form theory to our measurement data. In order to estimate c we use previously estimated values for γ_a, κ, μ and α. Assuming $\kappa \sim 33\,\text{GHz}$, $\mu \sim 2.29$, $\gamma_a \sim -0.5\,\text{GHz}$ and $\alpha \sim 2.8$ we estimate $c \sim 40\,\mu\text{W}$. Computed values can be obtained from table 4.1.

Fit of	P_x
$\kappa^2 \cdot P_{inj}/4$	$2.31 \cdot 10^3 \pm 0.80 \cdot 10^3\,\mathrm{GHz}^2$
γ_a	$-2.13 \pm 0.30\,\mathrm{GHz}$

Table 4.1: Computed values from fit of P_x using equation 2.4.

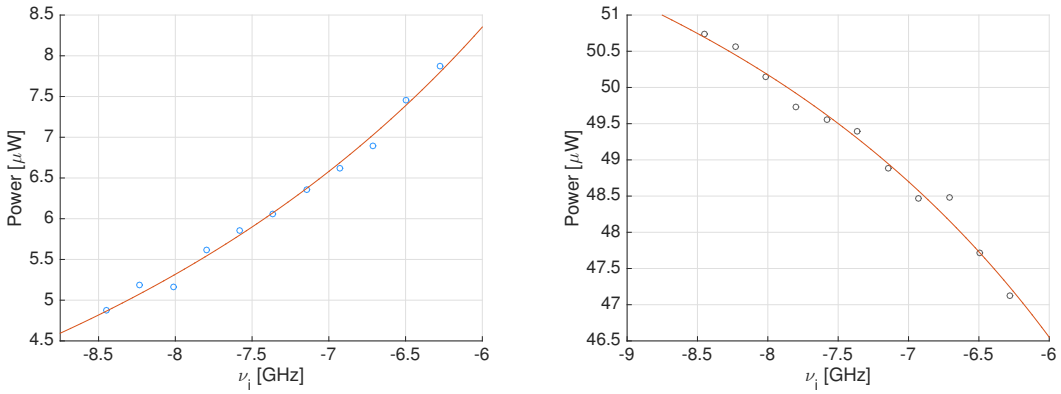

(a) Detail of the parallel polarisation, fit with equation 2.4

(b) Detail of the orthogonal polarisation, fit with 2.5

Figure 4.13: Power evolution over detuning for $P_{inj} = 151\,\mu$W, IL+PS regime only, Detail, fit with eq. 2.4 and 2.5, zoom of figure 4.10

A comparison of the IL+PS areas obtained for the variation of P_{inj} can be obtained from figure 4.14. Measurements for $P_{inj} = 151\,\mu$W, $78\,\mu$W and $39\,\mu$W are included. A measurement for $P_{inj} = 1322\,\mu$W is excluded because it gave inconclusive results on the boundaries of the region.

It is significant, that again we can see comparable values for the lower boundary of our region and decreased values in the bistable boundary to the IL region. This substantiates the theoretical assumptions. Furthermore the computed IL+PS area is nearly completely embedded in the area that was obtained for the variation of the injected power. The most probable reason for the IL+PS regime to be smaller than in the case of a constant detuning might lie in the measurement process. We denote a generally higher instability in the system for measurements of detuning variation, which could cause the system to switch into the IL state. Also the general measurement process is less stable. Due to internal jittering of the VCSEL and a slight instability of our tuneable laser a variation of ν_i is harder to implement than a variation of P_{inj}. It is also not possible to monitor detuning constantly over the measurement process. In order to obtain the steps of detuning which are taken, a step is set in the TL and the initial detuning is measured with the BOSA. Then the output is switched to the PMs and OSA, respectively. Data is taken according to the detuning values displayed by the TL. After the measurement is

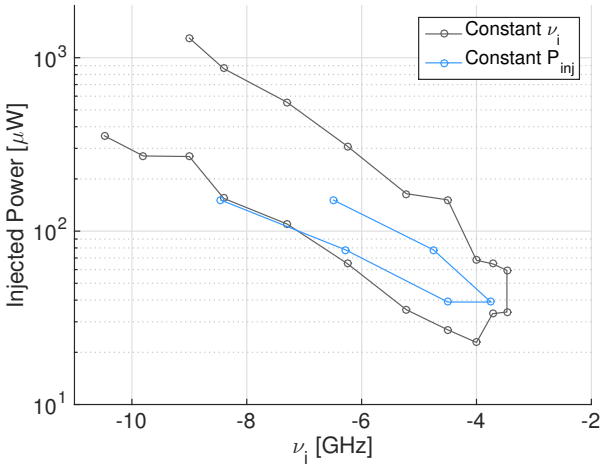

Figure 4.14: Map of the IL+PS region for $I = 3.05\,\text{mA}$ obtained by decrease of the detuning ν_i for fixed P_{inj} (blue) and P_{inj} for fixed detunings (grey).

completed detuning is measured again with the BOSA. If there are differences between the estimated and measured detuning, the measured detuning is chosen as the termination value. The process of connecting and disconnecting the fibers between the PMs and BOSA could have a so far unknown influence on the measurement parameters.

4.4 Dependence on the VCSEL Bias Current

Now we investigate the influence of the bias current of the VCSEL on the IL+PS region under parallel optical injection. We keep the setup similar and first fix a bias current of $I = 6.00\,\text{mA}$. Later we repeat the measurement for $I = 7.00\,\text{mA}$. Figure 4.15 shows a comparison of the theoretically obtained IL+PS areas for 3.05 and 6.00 mA by using the model of reference [14]. The theoretical curve for $I = 7.00\,\text{mA}$ can not be considered similar to the one for $I = 6.00\,\text{mA}$. We have seen in section 3.2.2 that a polarisation switching takes place. This switching will influence the γ_a significantly and hence we arrive to a different situation in the theoretical map, which is not given in this work. For simplicity we will just deal with qualitative phenomena in the case of $I = 7.00\,\text{mA}$. Deviations from $I = 3.05\,\text{mA}$ for the $I = 6.00\,\text{mA}$ case are a shift of the IL+PS area in the negative detuning domain to the left, hence the state is no longer visible for small negative detunings. We also see a broadening of this region, where the lower boundary stays constant but the upper, bistable boundary increases. In the positive domain we still expect to obtain the IL+PS state for detunings close to 0. The region broadens as both boundaries upper and lower increase. A stable IL+PS is expected for larger detuning values than before.

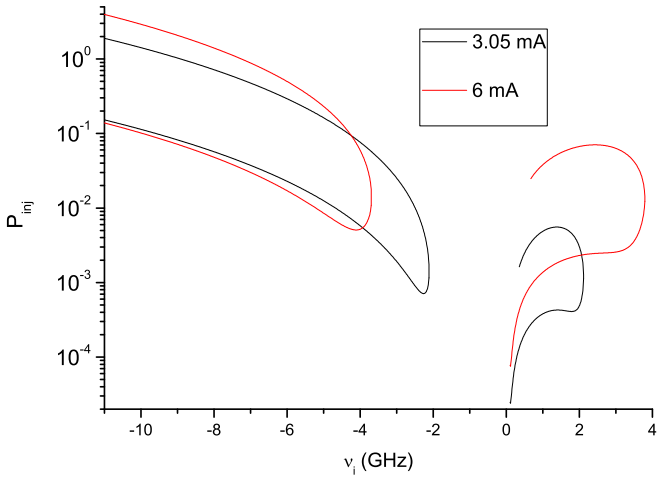

Figure 4.15: Theoretical map of the IL+PS region for $I = 3.05$ and $I = 6.00\,\text{mA}$.

In the case of $I = 6.00\,\text{mA}$ we conduct 4 measurements for each current, two in the positive and two in the negative region to characterise the behaviour of our system at this current. We choose again to increase the injected power for a constant detuning. In the IL+PS regime we see the same behaviour as for $I = 3.05\,\text{mA}$, illustrated in figure 4.16a. Linear fits for P_x and P_y give $R^2(P_\text{x}) = 0.9990$ and $R^2(P_\text{y}) = 0.9992$.

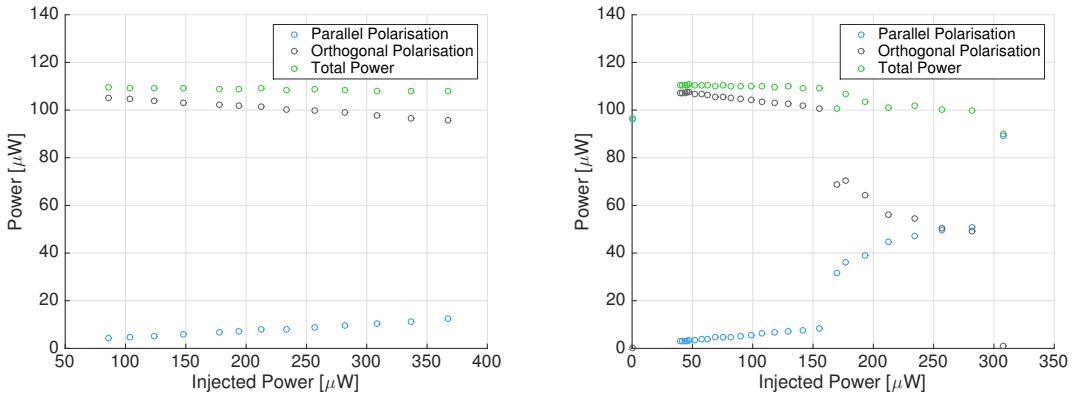

(a) $\nu_i = -6.1\,\text{GHz}$, IL+PS regime only

(b) $\nu_i = -5.2\,\text{GHz}$

Figure 4.16: Power evolution over injected power, parallel polarisation reflection reduced

Figure 4.16b illustrates how the evolution changes in the presence of another dynamical polarisation state. IL+PS is achieved for $P_\text{inj} \in [40, 155]\,\mu\text{W}$. For $P_\text{inj} \in [155, 281]\,\mu\text{W}$ the behaviour changes. P_tot is no longer constant but shows greater variation while P_x and P_y show curvature. Analysis of this behaviour in the BOSA showed that some kind of periodic dynamics are present in this region, before IL starts at $P_\text{inj} = 305\,\mu\text{W}$.

A map of the obtained IL+PS regions compared with the ones for 3.05 mA is given in figure 4.17. Our characterisation is consistent with theory. For a detuning of $\nu_i < -6.2\,\mathrm{GHz}$ we can no longer close the IL+PS region with our available injected power. For $\nu_i = -6.2\,\mathrm{GHz}$ we see a similar lower boundary of the region as for 3.05 mA and an increased upper boundary. This is again very consistent with previous results and our assumption of a bistability region at the upper boundary of the zone. For 5 GHz we measure similar values as for the 3.05 mA case. At $\nu_i = -4\,\mathrm{GHz}$ we can no longer see the IL+PS regime. This is consistent with an earlier closing of the area. For positive detunings we find strongly increased values for $\nu_i = +1.4\,\mathrm{GHz}$ compared to the situation for 3.05 mA. At $\nu_i = +2.9\,\mathrm{GHz}$ we measure a smaller IL+PS region again which is consistent with the fact that the maximum of the positive region has shifted. At $I = 3.05\,\mathrm{mA}$ it was not possible to measure any IL+PS state at this detuning value. The increase is consistent with figure 4.15. For $\nu_i \geq +4.0\,\mathrm{GHz}$ IL+PS is no longer present.

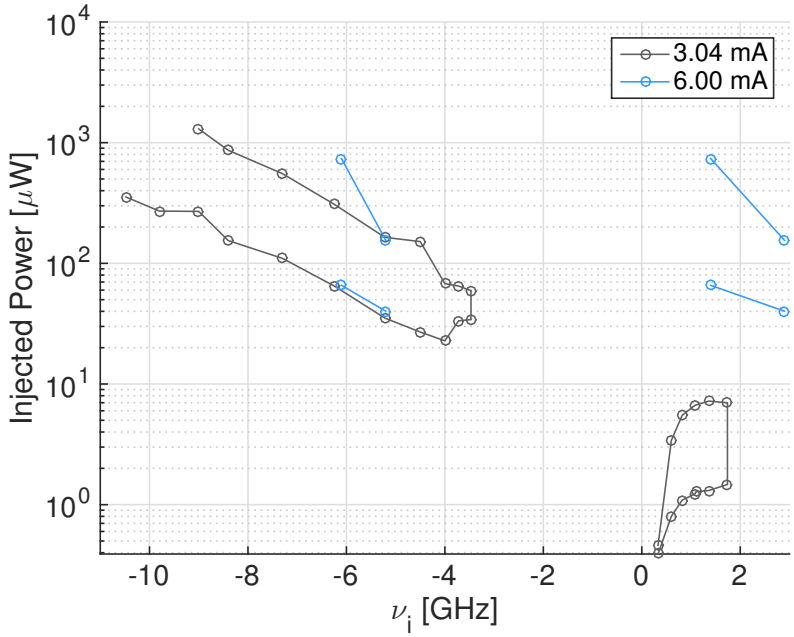

Figure 4.17: Map of the IL+PS region for $I = 3.05\,\mathrm{mA}$ (grey) and exemplary measurements at $I = 6.00\,\mathrm{mA}$ (blue), obtained by increasing P_{inj} for fixed detunings.

In the case of $I = 7.00\,\mathrm{mA}$ we have to consider the polarisation switching that takes place at $I \sim 6.5\,\mathrm{mA}$. Hence the orthogonal polarisation is the initially dominant one while the parallel is the inferior. Parallel and orthogonal are again defined as the one with the lower (parallel), respectively higher (orthogonal) frequency. We still consider parallel optical injection, which means injection parallel to the dominant polarisation. Hence now we inject with a detuning with respect to the orthogonal polarisation. Results for

the power evolution are shown in figure 4.18. Only negative detunings were investigated because for positive detunings too many regions of periodic dynamics in the spectra made the location of the IL+PS regime difficult. A detailed classification should be subject to further investigations.

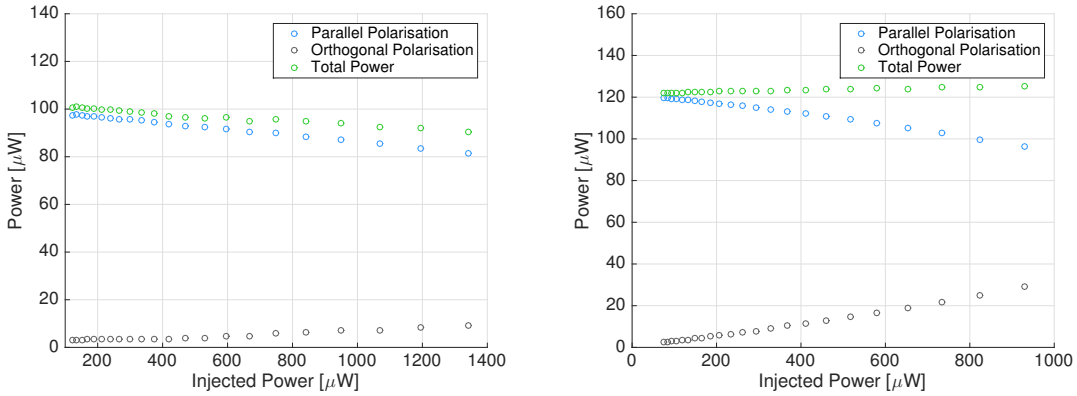

(a) $\nu_i = -5.8\,\mathrm{GHz}$ (b) $\nu_i = -5.1\,\mathrm{GHz}$

Figure 4.18: Power evolution over injected power $I = 7.00\,\mathrm{mA}$, IL+PS regime only, parallel polarisation reflection reduced

In the negative detuning domain we see similar behaviour as before. No IL+PS is found for detunings $\nu_i < 6.0\,\mathrm{GHz}$. Measurements for $\nu_i = -5.1\,\mathrm{GHz}$ (figure 4.18a) and $\nu_i = -5.8\,\mathrm{GHz}$ (figure 4.18b) are presented. The total power can be considered linear with deviations on the order of several percent. The dominant orthogonal polarisation is suppressed and linearly increasing with $R^2(P_\mathrm{y}, -5.2) = 0.9938$ and $R^2(P_\mathrm{y}, -5.8) = 0.9982$ while the parallel polarisation is the dominant one over the IL+PS region and linearly decreasing with $R^2(P_\mathrm{x}, -5.1) = 0.9955$ and $R^2(P_\mathrm{x}, -5.8) = 0.9524$. For $\nu_i = -4.5\,\mathrm{GHz}$ we can only observe dynamics.

5 Summary and Outlook

In this work we have conducted several measurements to classify the polarisation of a VCSEL subject to parallel optical injection under different conditions. First we have characterised our free-running VCSEL. Our VCSEL has a threshold current of $I_{\mathrm{th}} = 1.618 \pm 0.014\,\mathrm{mA}$ and saturation at about 9 mA. Our possible wavelength range is 1540 - 1544.5 nm, the birefringence of the device is 33 GHz. We find an internal quantum efficiency of $\eta = 0.1882 \pm 0.0006$ and a differential gain of $G_N = (1.64 \pm 0.2) \cdot 10^4\,\mathrm{Hz}$.

We inject light from a tuneable laser via a three port optical circulator into the VCSEL. Polarisation of the VCSEL output and the injected light is controlled by Fiber U-Bench polarisation controllers. The output is divided into a parallel and orthogonal polarisation part by a polarising beamsplitter. We analyse the output under three different conditions, first by keeping the detuning constant and changing the injected power, second by setting a constant injected power and varying the detuning and third by changing to different bias currents while keeping the detuning constant and modifying the injected power. For all measurements, unless denoted differently, we use $T = 25 \pm 0.05°\mathrm{C}$ and a bias current of $I = 3.05\,\mathrm{mA}$ as standard parameters.

At first we classify different behaviours of our system under variation of P_{inj} (for details, see figure 4.3). We find periodic dynamics and an excitation of the orthogonal polarisation, a suppressed free-running parallel polarisation along with an excited orthogonal, a new state where injection locking is achieved at the same time as polarisation switching (denoted as IL+PS) and complete injection locking (IL). This is the first time to our knowledge that the IL+PS state is observed and investigated. Next we analyse the output power evolution of our system for different constant detunings while varying the injected power. Before the IL+PS regime we find the parallel polarisation (P_{x}) and the total output power (P_{tot}) to be equal while the orthogonal (P_{y}) is completely suppressed. During the IL+PS regime the total power increases, P_{y} is at first completely excited and then decays linearly anticorrelated to P_{x} which is initially suppressed. We conclude that our system behaves according to our theoretical expectations. Following the theoretically estimated map of the output power evolution for several detunings we find similar behaviour. A complete map of the IL+PS region for P_{inj} up to $1.3 \cdot 10^3\,\mu\mathrm{W}$ and $\nu_i \in [-11, +2]\,\mathrm{GHz}$ is given (figure 4.7). Our map is in good qualitative agreement with the theoretical results. All previous measurements were obtained by increasing the injected power. In order to investigate the optical bistability of our system we map the IL+PS region for negative detunings while decreasing P_{inj}. We find the upper boundary of the IL+PS regime significantly shifted towards lower injection powers while the lower boundary can be considered approximately constant. This is in agreement with theoretical predic-

tions, which assume that bistability can be found in the transition between IL+PS and IL.

To further investigate the system bistability we set a constant bias current and vary the detuning. For the IL+PS regime we find again a constant total power and an initially excited P_y along with an initially suppressed P_x. This time we however expect a nonlinear decrease following equations 2.4 and 2.5. We can identify nonlinear behaviour for measurements of $P_{inj} = 39, 78$ and $151\,\mu$W. We present a map of the IL+PS region for this measurement in a range of $P_{inj} \in [39, 151]\,\mu$W and $\nu_i \in [-9, -3]\,$GHz (figure 4.14). We find again a decreased upper boundary and an approximately constant lower boundary. The total IL+PS region is however smaller, we think that this is related to a greater instability in measurements with changes in detuning.

In a third step we investigate changes in the IL+PS region arising form a change in bias current. Again we set a fixed detuning and increase the injected power. At $I = 6.00\,$mA we find a similar power evolution behaviour than for $I = 3.05\,$mA. We present a map of the estimated IL+PS region. Consistent with theory we see again an increase in the upper boundary and a constant lower boundary for negative detuings and an increase in both boundaries for positive detunings. Moreover we investigate the case of $I = 7.00\,$mA, where we find a different initial situation. Now P_y is the initially dominant polarisation while P_x is initially suppressed before the IL+PS regime. We now inject in the orthogonal polarisation, with a detuning with respect to P_y. We find qualitatively matching results for the power evolution in the negative detuning region.

In order to check the generality of our previously obtained results, we employ a different VCSEL with a birefringence of 12 GHz, hence about one third of the birefringence of the previous one. For detunings of $\nu_i = -7.4$ and $-4.1\,$GHz we can again identify polarisation switching and an IL+PS regime. Also a bistability in the IL+PS to IL boundary is again observed. The state could however not be identified for previous stability analysis of a VCSEL with a birefringence of 60 GHz [12].

Summarising, we have observed and investigated the IL+PS regime under several circumstances. Further investigations should consider other states such as period doubling or chaotic behaviour in order to classify them better. Better classification of the different states will lead to more accurate maps because one of our future objectives is the experimental and theoretical study of nonlinear dynamics of this system. Also a more detailed look at other devices with different birefringence would be desirable to classify the generality of our results.

Bibliography

[1] Iga, K.: Vertical-Cavity Surface-Emitting Laser: Its Conception and Evolution. In: *Japanese Journal of Applied Physics* 47, 1 (2008), S. 1–10

[2] Michalzik, R.: *VCSELs: Fundamentals, Technology and Applications of Vertical-Cavity Surface-Emitting Lasers*. Springer Verlag, 2013. – ISBN 978–3–642–24985–3

[3] Koyama, F.: Recent advances of VCSEL photonics. In: *Journal of Lightwave Technology* 24, 12 (2006)

[4] Demtröder, W.: *Experimentalphysik 3 - Atome, Moleküle und Festkörper*. Springer Verlag, 2005. – ISBN 3–540–21473–9

[5] Saleh, B. ; Teich, M.: *Fundamentals of Photonics*. John Wiley and Sons, 2007. – ISBN 978–0–471–35832–9

[6] Quirce, A.: *Doctoral Thesis: Dinámica de polarización y modos transversales de VCSELs sometidos a inyección óptica, Universidad de Cantabria*. 2012

[7] Pérez, P. ; Valle, A. ; Noriega, I. ; Pesquera, L.: Measurement of the Intrinsic Parameters of Single-Mode VCSELs. In: *Journal of Lightwave Technology* 32, 8 (2014), S. 1601–1607

[8] Noriega, I.: *Trabajo de Fin de Carrera: Medida de parámetros estáticos y dinámicos de un láser de semiconductor de emisión de cavidad vertical, Universidad de Cantabria*. 2015

[9] Moser, P. ; Lott, J.A. ; Wolf, P. ; Larisch, G. ; Li, H. ; Bimberg, D.: Temperature-Stable Oxide-Confined 980 Nm VCSELs Operating Error-Free at 46 Gb/s and 85° C. In: *2014 International Semiconductor Laser Conference* (2014)

[10] Ohtusbo, J.: *Semiconductor Lasers: Stability, Instability and Chaos*. Springer Verlag, 2013. – ISBN 978–3–642–30147–6

[11] Hurtado, A. ; Henning, I.D. ; Adams, M.J.: Differences in the injection locking bandwidth in 1550nm-VCSELs subject to parallel and orthogonal optical injection. In: *IEEE Journal Selected Topics in Quantum Electronics* 15, 19 (2009), S. 585–593

[12] Hurtado, A. ; Qurice, A. ; Valle, A. ; Pesquera, L. ; Adams, M.: Nonlinear dynamics induced by parallel and orthogonal optical injection in 1550 nm Vertical-Cavity Surface-Emitting Lasers (VCSELs). In: *Optics Express* 18, 9 (2010), S. 9425

[13] Quirce, A. ; Pérez, P. ; Popp, A. ; Valle, A. ; Pesquera, L. ; Hong, Y. ; Thienpont, H. ; Panajotov, K.: Two-Polarization mode emission in single-mode VCSELs subject to parallel optical injection. In: *Submitted to Optics Letters* (2016)

[14] Friart, G. ; Gavrielides, A. ; Erneux, T.: Analytical stability boundaries of an injected two-polarization semiconductor laser. In: *Physical Review* 91 (2015), S. 042918

[15] Pérez, P. ; A.Valle ; L.Pesquera: Polarization-resolved characterization of longwavelength vertical-vacity surface-emitting laser parameters. In: *Journal of the Optical Society of America B* 31,11 (2014), S. 2574–2580

[16] Deen, M. ; Kumar, S.: *Fiber Optic Communications: Fundamentals and Applications*. John Wiley and Sons, 2014. – ISBN 978–0–470–51867–0

[17] BeyondtechInc: *Fiber optic connector guide*. `http://beyondtech.us/blogs/beyond-blog/46105025-fiber-optic-connector-guide`. Version: December 2015

[18] AragonPhotonics: *Product descriptions: Bosa 100 and 200 Series*. `http://aragonphotonics.com/models/`. Version: December 2015

[19] OZ-Optics: *Product descriptions: Attenuators*. `http://www.ozoptics.com/products/attenuators.html`. Version: December 2015

[20] Estandía, S.: *Trabajo de Fin de Grado: Dinámica de Láseres de Semiconductor Sometidos a Retroalimentación Óptica, Universidad de Cantabria*. 2015

[21] Martin-Regalado, J. ; Prati, F. ; Miguel, M. S. ; Abraham, N.B.: Polarization Properties of Vertical-Cavity Surface-Emitting Lasers. In: *IEEE Journal of Quantum Electronics* 33, 5 (1997), S. 765–783